

Manipulating cavitation by a wall jet: experiments on a 2D hydrofoil

Timoshevskiy, Mikhail V.; Zapryagaev, Ivan I.; Pervunin, Konstantin S.; Maltsev, Leonid I.; Markovich, Dmitriy M.; Hanjalic, K.

DOI

[10.1016/j.ijmultiphaseflow.2017.11.002](https://doi.org/10.1016/j.ijmultiphaseflow.2017.11.002)

Publication date

2018

Document Version

Final published version

Published in

International Journal of Multiphase Flow

Citation (APA)

Timoshevskiy, M. V., Zapryagaev, I. I., Pervunin, K. S., Maltsev, L. I., Markovich, D. M., & Hanjalic, K. (2018). Manipulating cavitation by a wall jet: experiments on a 2D hydrofoil. *International Journal of Multiphase Flow*, 99, 312-328. <https://doi.org/10.1016/j.ijmultiphaseflow.2017.11.002>

Important note

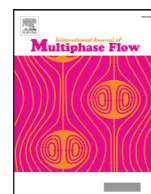
To cite this publication, please use the final published version (if applicable).
Please check the document version above.

Copyright

Other than for strictly personal use, it is not permitted to download, forward or distribute the text or part of it, without the consent of the author(s) and/or copyright holder(s), unless the work is under an open content license such as Creative Commons.

Takedown policy

Please contact us and provide details if you believe this document breaches copyrights.
We will remove access to the work immediately and investigate your claim.



Manipulating cavitation by a wall jet: Experiments on a 2D hydrofoil



Mikhail V. Timoshevskiy^a, Ivan I. Zapryagaev^a, Konstantin S. Pervunin^{a,b,*},
Leonid I. Maltsev^a, Dmitriy M. Markovich^{a,b,c}, Kemal Hanjalić^{b,d}

^a Kutateladze Institute of Thermophysics, Siberian Branch of the Russian Academy of Sciences (IT SB RAS) 1, Lavrentyev Ave., Novosibirsk 630090, Russia

^b Department of Physics, Novosibirsk State University (NSU) 2, Pirogov Str., Novosibirsk 630090, Russia

^c Institute of Power Engineering, Tomsk Polytechnic University (TPU) 30, Lenin Ave., Tomsk 634050, Russia

^d Faculty of Applied Sciences, Delft University of Technology (TU Delft), Building 58, Van der Maasweg 9, 2629 HZ, Delft, Netherlands

ARTICLE INFO

Article history:

Received 19 June 2017

Revised 19 October 2017

Accepted 1 November 2017

Available online 4 November 2017

Keywords:

Cavitation

Partial/cloud cavities

Instabilities

Flow control

Continuous tangential injection

Wall jet

Guide vane model

High-speed imaging

Time-resolved LIF visualization

PIV measurements

Pressure pulsations

Frequency spectra analysis

ABSTRACT

We report on the experimental investigation of cavitating flow control over a 2D model of guide vanes of a Francis turbine by means of a continuous tangential injection of liquid along the foil surface. The generated wall jet, providing supplementary mass and momentum, issues from a nozzle chamber inside the hydrofoil through a spanwise slot channel on its upper surface. High-speed imaging was used to distinguish cavity flow regimes, study the spatial patterns and time dynamics of partial cavities, as well as to evaluate the characteristic integral parameters of cavitation. Time-resolved LIF visualization of the jet discharging from the nozzle was employed to check if the generated wall jet is stable and spanwise uniform. Hydroacoustic measurements were performed by a hydrophone to estimate how the amplitudes and frequencies of pressure pulsations associated with cavity oscillations change with the injection rate. A PIV technique was utilized to measure the mean velocity, its fluctuations and the dominant turbulent shear stress component, which were all compared for different flow conditions and with the results for the unmodified (standard) foil. The effect of injection rate on cavitation and flow dynamics was examined for three attack angles, 0, 3 and 9°, and a range of cavitation numbers corresponding to different regimes. The low-speed injection was shown to lead to an intensification of turbulent fluctuations in the boundary layer and shrinking of the attached cavity length by up to 25% compared to the case without injection. The injection with a high velocity, in turn, causes a rise of the local flow velocity and a reduction of turbulent fluctuations near the wall, which, consequently, increases the foil hydrodynamic quality at a relatively low energy consumption for generation of the wall jet. However, in this case the vapor cavity becomes longer. Thus, the low-speed injection turns out to be effective to mitigate cavitation but the injection at a high velocity is more preferable from the standpoint of the flow hydrodynamics. In the whole, the implemented control method showed to be quite an efficient tool to manipulate cavitation and hydrodynamic structure of the flow and, thereby, under certain conditions, to suppress the cavitation-caused instabilities.

© 2017 Elsevier Ltd. All rights reserved.

1. Introduction

Active control and management of instabilities and inherent unsteadiness of various origins in hydrotechnical and hydropower equipment, hydraulic machinery and other flow systems has long served as an effective means for ensuring high efficiency, reliability and safety of their operation at off-design, transient or, for any reason, suboptimal regimes. The main challenge is to suppress the growth of amplitudes of flow-rate and pressure pulsa-

tions and, thereby, functional stresses on components of hydraulic machinery. This applies also to cavitation, which is one of the most widespread and dangerous sources of flow instabilities. In order to control cavitation, various means of flow manipulation can be applied to the elements of a hydraulic system, which can diminish the noise level and vibrational loads on the supporting framework and, thus, eliminate or at least partially reduce the risks of the occurrence of resonance phenomena. The management of cavitation processes is essential both for hindering the development of cavitation itself and for preventing or diminishing its negative impact. This calls for thorough studies of the causes and mechanisms of the unsteadiness and its evolution, and their roots in the fundamental physics of the phenomenon of cavitation. In parallel, there are urgent needs for the development of methods to effec-

* Corresponding author at: Kutateladze Institute of Thermophysics, Siberian Branch of the Russian Academy of Sciences (IT SB RAS) 1, Lavrentyev Ave., Novosibirsk, 630090, Russia.

E-mail address: pervunin@itp.nsc.ru (K.S. Pervunin).

tively control cavitating flows, which should lead to further improvements and optimization of the design and operating conditions of up-to-date hydraulic machinery.

It is well known (Kjeldsen et al., 2000; Watanabe et al., 2001; Kawakami et al., 2008) that, under certain conditions, attached cavities become unstable. According to the modern classification (Callenaere et al., 2001), there are two primary types of partial cavity instabilities. If the instability is generated by the cavity itself, it is called intrinsic, but if it is caused by the interaction of the cavity with other cavities or elements of a hydraulic system, especially its inlet and outlet ducts, it is regarded as system instability. For example, the well-studied cloud cavitation that is characterized by auto-oscillations of the sheet cavity length and quasi-periodical shedding of cloud cavities occurs for the cavities of moderate lengths (40–60% of an object extension) and is governed by the development of an intrinsic instability – a re-entrant jet moving upstream underneath the attached vapor cavity (Kubota et al., 1989; Brandner et al., 2010; Peng et al., 2016) or bubbly shocks propagating in high-void-fraction bubbly mixtures in the separated cavity region (Reisman et al., 1998; Ganesh et al., 2016). The only requirement for this type of instability to develop is that the attached cavity thickness must be noticeably larger than the one of the jet. In case of a bubbly mixture, the thickness of the propagating discontinuity is equal to that of the cavity. The most prevalent case of system instabilities is so called cavitation surge (see description in Callenaere et al., 2001; Duttweiler and Brennen, 2002; Iga et al., 2011) that is common for relatively long and thin cavities (with length in the range of 75–100% of a test body chord and thickness comparable with that of the re-entrant jet, though the jet itself does not exist in this case). If so, auto-oscillations of the cavity length are conditioned by the propagation of pressure waves along the test channel. Besides, spectra of pressure pulsations relevant to the intrinsic and system instabilities differ substantially: the former occur at frequencies two or even more times higher than those for the latter.

Control of cavitation inception and development can be achieved by both active and passive methods. At present, there are several promising approaches of active management of cavitating flow based on diverse underlying principles, some of proved efficiency in practice. The most known among them are the control of cavitation nuclei number by means of ultrasound or electrolysis (Chatterjee et al., 1997, 2004), injection or suction of a liquid (Chang et al., 2011), polymer solution (Chahine et al., 1993; Chang et al., 2011) or gas (Mäkiharju et al., 2015) through the surface of a test object and forced boundary layer transition to turbulence by applying external disturbances (Franc and Michel, 1988). In all passive methods, cavitation control is realized by modifying wall properties in one way or another, without energy supply to the flow: selection of a material with certain attributes (Tassin Leger and Ceccio, 1998), patterning of irregular (Coutier-Delgosha et al., 2005; Churkin et al., 2016) or regular (Kawanami et al., 1997; Ausoni et al., 2012; Danlos et al., 2014) roughness and use of flexible coatings (Akcabay et al., 2014; Zarruk et al., 2014; Wu et al., 2015). However, one of the simplest in implementation and effective techniques of flow control is likely to be a continuous tangential liquid injection along the surface of the test body to feed the boundary layer with additional momentum to overcome adverse pressure gradient (Kozhukharov et al., 1985). Nonetheless, extensive information on using this approach to manipulate cavitation is scarce in the literature.

This paper aims at experimental verification of a possibility to control cavitation and turbulent structure of the flow by generating a wall jet along the suction side of a test hydrofoil through a spanwise slot channel in the surface and assessment of its effectiveness for partial cavity flow manipulation. The present study is based on an analysis of visual observations of partial cavities

Table 1

Points of the generatrix of the guide vane (GV) surface at different cross-sections x along its chord. y_{up} and y_{down} are the transversal coordinates of these points at the upper (with slot) and lower (w/o slot) surfaces with respect to the hydrofoil chord (zero line). The GV thickness in every cross-section is $H(x) = y_{up} - y_{down}$. The shape of the GV model is a cubic spline approximation of these values.

x/C	y_{up}/C	y_{down}/C
0	0	0
0.1	0.0658	-0.0658
0.2	0.0898	-0.0898
0.3	0.1045	-0.1045
0.4	0.1098	-0.1098
0.5	0.1087	-0.1087
0.6	0.0925/0.0845	-0.0981
0.7	0.0713	-0.0792
0.8	0.0544	-0.0554
0.9	0.0312	-0.0312
1	0.0065	-0.0065

gathered by high-speed imaging, information from power spectra of pressure pulsations caused by cavitating flow unsteadiness and PIV measurements of spatial distributions of the mean velocity and turbulent characteristics. The results are compared with those for a standard (i.e., without slot) hydrofoil of the same chord length.

2. Experiment

2.1. Experimental setup, test object and control system

The experiments were carried out in the cavitation tunnel in Kutateladze Institute of Thermophysics SB RAS. An explicit description of the test rig and experimental conditions can be found in Kravtsova et al. (2014). The test object was a scaled-down model of guide vanes (GV) of a Francis turbine with the chord length $C = 100$ mm. The GV section was equipped with a spanwise slot channel in its upper surface, through which liquid was injected in form of a wall jet, so that the hydrofoil remained two-dimensional but asymmetric. Fig. 1 shows its shape and a schematic of flow organization. The GV profile can be reconstructed using the generatrix data given in Table 1. Apart from the slot, which itself (without jet) can affect the flow conditions, the GV model was made as close as possible to its original geometry. It has a blunt trailing edge (which is typical for full-scale guide vanes) with a thickness of 1.3 mm unlike the sharp one used in our previous study (Timoshevskiy et al., 2016). The maximum thickness of GV was $H^{max} = 0.2206C$ in the cross-section $x^{max}/C = 0.4396$ measured from its leading edge (see Fig. 2). The GV aspect ratio was $S/C = 0.8$, where $S = 80$ mm is the foil span that is equivalent to the width of the test channel (with 250×80 mm cross-section). Its rotating axis was somewhat shifted toward the trailing edge with respect to the foil geometric center and was located at a distance of $0.54C$ from its leading edge. The GV model was supported as a cantilever on one of the test section sidewalls adjoining tightly to both of them, with the distance between the test section inlet and the hydrofoil axis being 755 mm. The hydrofoil was manufactured of brass with the mean level of surface roughness of about $1.5 \mu\text{m}$. The investigation was performed for the attack angle α of 0, 3, 9 and 12° . In order to achieve diverse cavitation regimes in the experiments, the cavitation number $\sigma = (p_0 - p_v) / (\rho U_0^2 / 2)$ was varied by changing the static pressure p_0 and/or the mean flow velocity U_0 . Note that p_v is the saturation vapor pressure of the operating liquid (distilled water) and ρ is the liquid density.

As mentioned above, in order to manipulate the flow, the GV foil was equipped with a spanwise slot channel that is the exit section of the spanwise-uniform nozzle located inside the GV. The operating liquid was supplied by means of a centrifugal pump or

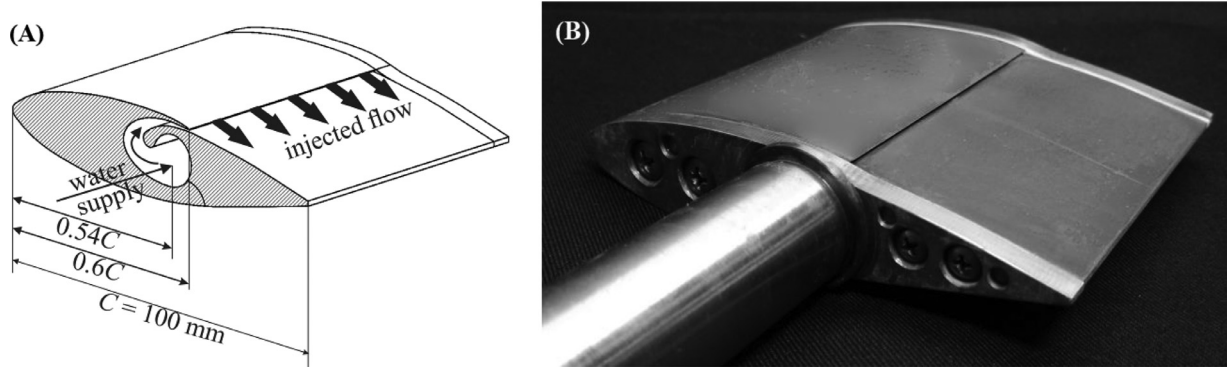


Fig. 1. (A) 3D schematic and (B) photo of the fabricated guide vane (GV) model with a rotary-fixing element attached. The maximum GV thickness of $H^{\max}/C = 0.2206$ is reached at the distance of $x^{\max}/C = 0.4396$ from its leading edge. The rounding radius of the foil leading edge is 1.97 mm, the height of the blunt trailing edge is 1.3 mm.

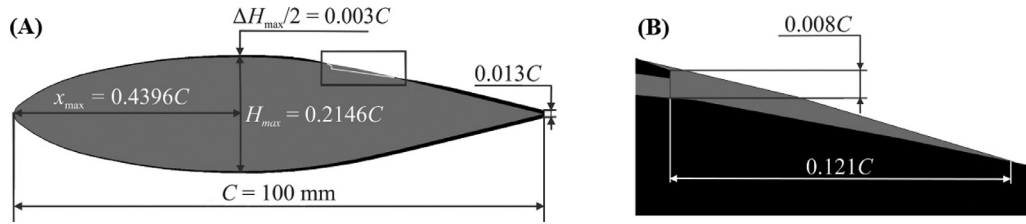


Fig. 2. Comparison of the two shapes of the GV model: (A) the full-length image and (B) the blow-up of the near-slot region corresponding to the box-shaped area in image (A) with inverted overlapping of the foil diagrams. The black sketch corresponds to the modified GV section with the slot channel on the upper surface and the blunt trailing edge, whereas the grey one is for the standard GV profile with the sharp trailing edge from Timoshevskiy et al. (2016).

driven by a natural pressure gradient from a bypass circuit directly into the inner nozzle along a pipeline with the inner diameter of 13 mm that passed within a rotary-fixing element (extension of the rotating axis) of the GV profile and then released into the main flow through the slot channel. In the bypass circuit, the liquid was sucked in upstream of the honeycomb of the major loop of the experimental rig. The liquid from the bypass line was partially supplied to the test section and the rest of it was returned back into the facility, immediately in front of the entrance to the pumping group, so the total amount of the operating liquid in the tunnel was constant. The nozzle chamber inside the hydrofoil was of a helical configuration contracting to the outlet (Fig. 1-A). The contraction ratio of the nozzle (i.e., the ratio of its intake area to the discharge one) equals to 3.16. The outlet cross-section of the slot nozzle was $h_N = 0.6$ mm in height and $a_N = 70$ mm in width and was located at the distance of $0.6C$ from the GV leading edge. Thereby, the liquid was injected across the entire span of the vane excluding two end caps (each of 5 mm width). The height of the 'backward-facing step' (i.e., the overall vertical dimension of the slot and the lip) was 0.8 mm (see details in Fig. 2). In the experiments, the liquid flow rate through the slot channel did not exceed 0.7 l/s (measurement uncertainty of 2%), which corresponded to the maximum injection velocity of the generated wall jet of $U_{inj} = 16.7$ m/s. The nonuniformity of the velocity profile of the wall jet along the slot nozzle (in the spanwise direction) is assessed to be within 5% (based on the maximum value) for $U_{inj}/U_0 > 0.15$. If the injection rate is lower than this threshold, the profile nonuniformity progressively increases with decreasing the jet velocity but does not exceed 30%.

The injection rate is the key parameter that (in addition to the attack angle α and the cavitation number σ) governs the flow and the cavitation regime. It needs to be defined in a general manner that could be used to scale-up and extrapolate the laboratory results obtained on simplified and idealized flow models to real situations. The simplest and most practical criterion is the ratio of the velocity of the injected liquid to the mean flow ve-

locity U_{inj}/U_0 , which can give an indication of the ability of the wall jet to overcome the adverse pressure gradient, for instance when $U_{inj}/U_0 \geq 1$. However, physically more appropriate one is, perhaps, the momentum ratio of the wall jet and the oncoming flow. This has been labelled as the jet momentum coefficient C_μ (e.g., Kozhukharov et al., 1985), which identifies the momentum (and, indirectly, the amount of energy) spent to produce the wall jet with respect to that of the main flow. The coefficient C_μ can serve for a quantitative assessment of the power of the controlling flow. Depending on the considered flow parameters, this coefficient can be expressed in different ways. In this study, it was defined as the ratio of the momentum input through the slot channel to the momentum imparted to the hydrofoil by the primary flow due to its blocking according to the following formula:

$$C_\mu = \frac{m_{inj} U_{inj}}{m_0 U_0} = \frac{U_{inj}^2 S_N}{U_0^2 S_M} = \frac{U_{inj}^2 h_N a_N}{U_0^2 h a},$$

where m_{inj} is the mass flowrate of liquid discharging from the slot channel with the outlet cross-section area S_N , m_0 is the equivalent mass flowrate of liquid of the main flow that would pass through the frontal (midsection) area S_M of the hydrofoil in case of its absence, h is the height of the GV midsection, i.e. the section where the foil projection onto the y -axis depending on the attack angle α takes its maximum value ($h = H^{\max}$ at $\alpha = 0^\circ$). Here, C_μ can be regarded to be approximately equal to $0.024 U_{inj}^2/U_0^2$ for all the considered attack angles α because of their relative smallness.

2.2. Measurement and visualization techniques

In the present research, we used a high-speed imaging to study dynamics and spatial patterns of partial cavities or transient bubbles on the foil suction side and evaluate their integral parameters, such as the maximum (for unsteady regimes) and average (for steady flow conditions) length of a cavitation area, periods of attached cavity oscillations, characteristic frequencies of cloud shedding process and the maximum size of travelling bubbles. The visualization was performed at the sampling rate of 20 kHz with an

optical magnification of 0.11. In order to measure flow velocity over the suction side of both hydrofoils and quantify the mean and turbulent flow characteristics, a two-dimensional PIV method with an optical magnification of 0.11 and a high spatial resolution (0.52 mm square for each velocity vector) was employed. These two methods are comprehensively described in Kravtsova et al. (2014) along with the details on calculation and validation of the velocity fields and assessment of the measurement uncertainties for different turbulence characteristics. In addition to high-speed imaging and PIV measurements, the wall jet was visualized by laser-induced fluorescence (LIF) with a high temporal resolution (10 kHz) and hydroacoustic signals were analyzed to determine the dominant frequencies of pressure variations associated with attached cavity oscillations and periodic cloud shedding.

For the wall jet visualization, water dyed with Rhodamine 6G was injected from a pressurized tank into the bypass circuit and then led to the nozzle settling chamber. The flow rate of water with the dissolved fluorescing paint did not exceed 30 l/h and was varied to adjust the dye concentration in the jet to 50–150 µg/l, depending upon the injection rate (the jet velocity). The flow rate was controlled by changing the pressure difference between the tank and the bypass line and was determined by measuring the change of the water level in the pressurized tank with time. In order to illuminate the wall jet, we used a PIV-system with a high temporal resolution consisting of a pulsed Nd:YAG Photonics Industries DM-532-50 laser (wavelength 532 nm, repetition rate 10 kHz, pulse energy 7 mJ, pulse duration 190 ns) with laser beam optics, a high-speed Photron FASTCAM SA5 CMOS-camera (digit capacity 12 bits, resolution 1024 × 1024 pix., acquisition rate 7 kHz) equipped with a Nikon AF Micro-Nikkor 200 mm f1/4D IF-ED lens and a low-pass optical filter (transmission edge at 570 nm) and a Berkeley Nucleonics Corporation pulse/delay generator (model 575) for external synchronization. The optical magnification of the measurement system was 0.6. The LIF visualization was performed in two configurations. In the first one, the camera line of sight was perpendicular to the laser light sheet as in the conventional 2D PIV technique to check how stable the wall jet generation is and to observe the dynamics of vortical and cavitation structures. In the second configuration, the laser beam was swept over the area of 7 mm streamwise and 70 mm spanwise dimension on the GV surface including the slot channel. The camera was shifted upward compared to the previous configuration and inclined at 25° angle to the hydrofoil plane at zero attack angle to verify the spanwise uniformity of the jet flow.

Local pressure was recorded in the wake of both GV profiles by means of a hydroacoustic pressure transducer flush-mounted into the sidewall of the test section using wax as a sealant. The transducer used is a hydrophone Brüel&Kjær Type 8103 (sensor diameter – 9.5 mm, voltage sensitivity – 24.6 µV/Pa, measurement frequency range – from 0.1 Hz to 180 kHz, frequency response – +3.5 dB for 0.1 Hz and –14 dB for 180 kHz (re 250 Hz), measuring uncertainty – ±0.25 dB at 250 Hz). It was positioned at the center of the test section in the vertical direction and 80 mm shifted behind the GV trailing edge to record hydroacoustic signal in the wake of both hydrofoils and derive power spectra of pressure pulsations. The sidewall at which the hydrophone was fixed is a black-colored duralumin plate of 10 mm thickness that is vibrationally isolated by rubber pads from the resting part of the test section and the experimental facility as a whole. Pressure variations inside the slot nozzle chamber were registered by a piezoresistive pressure transmitter with an open diaphragm Keller PAA-25 (sensor diameter – 15 mm, pressure limits – 0–4 bars, sampling rate – 10 kHz, measurement uncertainty – 0.25%) that was installed at the end of the rotary-fixing element of the modified GV foil. The sampling rate of the both pressure sensors was 10 kHz during the tests, so their maximum measured frequency was 5 kHz.

Table 2

Absolute and relative errors in determining the cavitation number for the maximum and minimum mean flow velocities at the two angles of attack provided that $\delta U = 2\%$ on the average.

Flow parameters	$\alpha = 3^\circ$		$\alpha = 9^\circ$	
U_0 , m/s	11.7	13.1	8.9	11
p_0 , kPa	91	74	116	98
σ	1.26	0.82	2.82	1.56
$\Delta\sigma$	0.072	0.05	0.15	0.088
$\delta\sigma = \Delta\sigma/\sigma$	5.7%	6.1%	5.3%	5.6%

2.3. Instrumentation and measurement uncertainties

The foil inclination was determined using an optical quadrant with the measurement uncertainty of $0^\circ 0' 30''$, which allowed us to set the attack angle manually with a precision within about 0.1° , the main inaccuracy originating from the error in positioning the zero level. The static pressure p_0 was measured at a sidewall of the test channel near its inlet by a diaphragm strain-gauge pressure transducer with imprecision of $\Delta p = 1.5$ kPa.¹ During the tests, the water temperature was kept at 30°C with uncertainty of $\pm 0.1^\circ\text{C}$ by means of a thermoregulator consisting of a copper 50 Ohm resistive temperature transducer, a cooling circuit and an electromagnetic valve that was activated by a PID-control unit to start/stop coolant supply to the cooling circuit. The saturation vapor pressure p_V at this temperature was found in the reference book (Dean, 1999) to be equal to 4.24 kPa. As the variations in the water temperature are very low, the vapor pressure can be regarded as constant.² The mean flow velocity U_0 was measured by PIV in the central vertical longitudinal section of the test channel (from top to bottom) close to its inlet. The typical measurement error of the cross-correlation procedure used in the PIV approach does not exceed 0.1 pixel for a 32×32 pixel interrogation area, which corresponds to $\delta U = 1\%$ and 4% for the particle displacements of 8 and 2 pixels, respectively (see details in Kravtsova et al., 2014). The measurement uncertainty of the Reynolds number that is based on the foil chord length and the mean flow velocity is directly proportional to δU and equals roughly 2% since, for the measured velocity fields, $\delta U \approx 2\%$ on the average. Thereby, the inaccuracy in determining the cavitation number can be expressed as follows:

$$\Delta\sigma = \frac{2}{\rho U_0^2} \left(\Delta p \mp \frac{2\Delta U}{U_0} [p_0 - p_V] \right) = \frac{2}{\rho U_0^2} (\Delta p \mp 2\delta U [p_0 - p_V]).$$

The assessed values for the limiting mean flow velocities (i.e., its maximum and minimum values at the incidence angle of 3 and 9°) are presented in Table 2. So, the cavitation number was ascertained within a precision of nearly 6%.

The estimated measurement uncertainties of the integral parameters of partial cavities and transient bubbles extracted from the visual data are presented below. The imprecision in evaluation of the size of travelling bubbles was 2 pixels or 0.36 mm for the spatial resolution of 0.18 mm per pixel. The sheet cavity length L_C was measured with a higher inaccuracy of $\Delta L_C = 15$ pixels or 2.7 mm with respect to the transient bubble diameter for the same spatial resolution because of spanwise variations of the cavity terminus and shedding of relatively small clouds from its closure. The Strouhal number $St = fC/U_0$ that corresponds to the frequency of sheet cavity oscillations or cloud shedding can be found from the

¹ Hereinafter, we imply that Δ relates to absolute error while δ denotes relative one.

² This is admissible since, when the temperature changes even by two degrees from 29 to 31°C , p_V alters only from 4.01 to 4.49 kPa, which is too small to affect the experimental data.

Table 3

Absolute and relative errors in determining the Strouhal number for the maximum and minimum frequencies of sheet cavity length pulsations (or cloud shedding) at the two angles of attack provided that $\delta U = 2\%$ on the average.

Flow parameters	$\alpha = 3^\circ$		$\alpha = 9^\circ$	
f , Hz	18	26	18	135
T , ms	55.6	38.5	55.6	7.4
U_0 , m/s	13.1	13.1	11	11
St	0.14	0.2	0.16	1.23
ΔSt	0.004	0.007	0.005	0.116
$\delta St = \Delta St / St$	2.9%	3.5%	3.1%	9.4%

visual data with the following uncertainty:

$$\begin{aligned} \Delta St &= \frac{C \Delta f}{U_0} \mp \frac{C f \Delta U}{U_0^2} = \frac{C}{U_0} (\Delta f \mp f \delta U) \\ &= \frac{C}{U_0} \left(\frac{\Delta T}{T^2} \mp \frac{\delta U}{T} \right) = \frac{C}{U_0 T} (\delta T \mp \delta U). \end{aligned}$$

Table 3 displays the absolute and relative errors in determining the Strouhal number. The results shown take into account that the moment of breakdown of an attached cavity interface can be determined visually with an inaccuracy of $\Delta T = 11$ frames or 0.55 ms for the interframe interval of 50 μ s (the acquisition rate of 20 kHz) which arises due to the cavity detachment occurring non-simultaneously over the hydrofoil span. Thus, the Strouhal number of cavity length oscillations (or cloud shedding) can be estimated with a relative error not exceeding 4% for large-scale cavity length pulsations that are typical for cloud cavitation or cavitation surge and within 10% for short cavities characterized by high-frequency shedding of relatively small clouds. The other quantities used for data analysis in the current research are derivatives of those described above. So, their measurement errors can be expressed as a superposition of the uncertainties of their components.

3. Results

We present here a selection of results of the experimental study on manipulation of cavitating flow over the GV model by a wall jet at the attack angles $\alpha = 3^\circ$ and 9° in comparison with the results for the standard (i.e., unmodified) hydrofoil. The geometry of the latter was specified in Timoshevskiy et al. (2016). The section is divided into three subsections. In the first two, experimental data for the smaller ($\alpha = 3^\circ$) and larger ($\alpha = 9^\circ$) foil inclinations are presented, whereas in the third subsection a brief summary is given of the discovered effects of the wall jet on the cavitating flow, together with an assessment of the effectiveness of the implemented flow-control method. In the first and second subsections, we distinguish four flow regimes on the cavitation number some of which are dependent upon the injection velocity: single-phase flow, travelling bubbles or cavitation sheet, transitional cavities and unsteady cavitation. The governing parameters for all flow conditions considered in the study are listed in Table 4. For each regime except for travelling bubbles at $\alpha = 3^\circ$ and transitional cavity at $\alpha = 9^\circ$, we first compare the cavitation patterns, turbulent structures and power spectra of the pressure variations (only in unsteady regimes) for the standard and modified GV profiles under unforced flow conditions (i.e., without injection) and then ascertain how they change as the injection velocity is increased. The cavitation patterns captured by high-speed imaging are used to recognize the cavitating flow regime, examine spatial structure of cavitation, qualitatively estimate spatial density of transient bubbles and measure the integral characteristics of partial cavities and travelling bubbles. Visual observations by high-speed LIF are needed to trace the development of the generated wall jet and verify whether it is stable in time and spanwise uniform. Turbu-

lent flow structures are discussed based on the two-dimensional distributions of the streamwise components of the mean velocity and turbulent characteristics by way of turbulence intensity and the Reynolds stresses nearby the GV surface.

Figs. 3 and 7 show distributions of the streamwise component of the time-averaged velocity in the form of velocity defect $(U - U_0)/U_0$, the streamwise *rms* (root-mean-square) component of the fluctuating velocity \tilde{u}/U_0 and the Reynolds shear stress $\langle uv \rangle / U_0^2$ in several cross-sections along the GV surface baseline projected onto the foil chord. So, the x -axis is directed streamwise, independent of the attack angle α , and the y -axis is always orthogonal to the flow direction. In every cross-section, $y/C = 0$ corresponds to a point on the upper (with a slot) side of the GV foil. The origin of coordinates ($x/C = 0$, $y/C = 0$) coincides with the GV leading edge at the attack angle $\alpha = 0^\circ$ in the measurement plane. Thus, the slot channel is positioned at the point ($x/C = 0.6$, $y/C = 0$). In order to facilitate a direct comparison, all plots are presented together for both modifications of the GV model and different U_{inj}/U_0 . The interfacial boundaries of the attached cavities extracted from the visual data are depicted in the graphs as solid and dashed lines for different injection rates. Below, we define the boundary layer (BL) thickness δ_{BL} as the distance from the foil surface along the y -coordinate at which the mean velocity is less than or equal to 0.95 of that at infinity. As said above, the visual data (see Figs. 4 and 8) are used to evaluate the integral parameters of partial cavities and travelling bubbles. To estimate the maximum cavity length for unsteady flow conditions, we applied the following criterion: the bulk of the cavity interface must remain glossy (undisturbed) so that no breakup of the cavity interface or shedding of even small clouds from the cavity closure could be observed. The spanwise dimension of the cavitation area in case of travelling bubbles was determined as a longitudinal extent from an imaginary transverse line at which the transient bubbles arise to the one at which they collapse. Periods of attached cavity length pulsations were measured as time intervals between the consecutive moments of the cavity detachments or collapses.

3.1. Small attack angle ($\alpha = 3^\circ$)

3.1.1. Cavitation-free flow

In the subcavitating case ($\sigma = 1.26$) at $\alpha = 3^\circ$, the intensity of turbulent fluctuations in the boundary layer (BL) unexpectedly turns out to be more than 60% higher for the standard GV ($\tilde{u}/U_0 = 0.176$ at $x/C = 1$, $y/C = 0.023$) compared to the modified foil without injection ($\tilde{u}/U_0 = 0.108$ at the same point) (see Fig. 3-B.1), although the shape of the modified GV is obviously less streamlined. This circumstance is presumably conditioned by the difference in geometries of both hydrofoils (mainly by the presence/absence of the slot nozzle, Fig. 2-A). Indeed, for the modified GV, after the BL separation from the ‘backward-facing step’ formed by the slot channel and its lip the flow reattaches in a laminar manner to the GV surface downstream, admittedly forming a recirculation zone between the nozzle exit and the reattachment point. However, since the rear part of the modified GV is thicker (between the cross-sections $x/C = 0.72$ and 1.0, Fig. 2) and, therefore, the adverse pressure gradient is lower in this region, turbulence of the BL on the GV model with the slot occurs slower. Once the liquid injection with a low ($U_{inj}/U_0 < 1$) relative velocity is started, it causes a significant augmentation of the modulus of the mean velocity defect near the trailing edge ($x/C = 1$) of the modified GV section. For instance, when $U_{inj}/U_0 = 0.64$ ($C_\mu = 0.01$), the mean velocity defect increases from $|(U - U_0)|/U_0 = 0.59$ for the unforced flow conditions (i.e., without injection) up to 0.85. So, their difference is $\Delta U/U_0 = 0.26$ (Fig. 3-A.1), though the BL thicknesses in both cases are equal to $\delta_{BL} \approx 0.05C$. In addition, when the injection takes place, turbulent fluctuations grow above the foil termi-

Table 4

Summary of the regimes for the modified GV model considered in the study in comparison with those for the unmodified one.

Flow conditions		U_{inj}/U_0	C_μ	L_c^{max}/C^a	D_B , mm	St		
α , °	σ / regime							
3	1.26 subcavitating flow	standard		no cavitation	no bubbles	steady regimes		
		0	0					
		0.32	0.002					
		0.51	0.006					
		0.64	0.01					
		1.07	0.028					
	0.93 travelling bubbles / transitional regime	1.32	0.042					
		standard		0.51	2.6			
		0	0	0.47	1.9			
		0.23	0.001	0.46	3.4			
		0.43	0.004	0.47	4.5			
		0.65	0.01	0.44	4.3			
		0.79	0.015	0.46	5.4			
		0.93	0.02	0.48	4.7			
		1.09	0.028	0.49	3.4			
		1.26	0.038	0.5	2.9			
	0.87 transitional regime / cavitation surge	standard		0.57	1.5	0.1		
		0	0	0.51	1.6	0.08		
		0.24	0.001	0.46	2.3	steady regimes		
		0.49	0.006	0.51	2.9			
		0.73	0.013	0.52	3.1			
		0.85	0.017	0.53	3.6			
		0.97	0.023	0.54	3.3			
		1.07	0.028	0.55	2.7			
		1.28	0.039	0.59	2.6			
		0.82 cavitation surge	standard		0.6	1.8	0.1	
	0		0	0.58	1.6	0.09		
	0.25		0.002	0.52	1.7	0.09		
	0.5		0.006	0.53	2.1	0.09		
	0.75		0.013	0.56	2	0.085		
	0.86		0.018	0.62	2.1	0.1		
	0.96		0.022	0.61	2.1	0.1		
	1.1		0.029	0.68	2.3	0.1		
	1.25		0.037	0.7	1.8	0.1		
	9		2.82 subcavitating flow	standard		no cavitation	no bubbles	steady regimes
		0		0				
		0.22		0.001				
		0.45		0.005				
		0.67		0.011				
		1.12		0.03				
		1.35		0.044				
		1.49		0.053				
		1.66		0.066				
		2.17 subcavitating flow / sheet cavity		standard		0.08		
				0	0	0.13		
0.045				$4 \cdot 10^{-5}$	0.03			
0.21				0.001	0			
0.41				0.004	0			
0.66			0.01	0				
1.07			0.028	0.17				
1.29			0.039	0.21				
1.38			0.046	0.23				
1.55			0.058	0.27				
1.96 sheet cavity		standard		n/a				
		0	0	0.38				
		0.13	0.0004	0.37				
		0.26	0.002	0.33				
		0.46	0.005	0.32				
		0.59	0.008	0.35				
		0.85	0.017	0.38				
		1.04	0.026	0.37				
		1.24	0.037	0.39				
		1.48	0.053	0.41				
1.56 unsteady intermittent cavitation		standard		0.3-0.7		0.16-0.49		
		0	0	0.3-0.67		0.14-0.5		
		0.18	0.001	0.46-0.67		0.14-0.5		
		0.39	0.004	0.4-0.65		0.14-0.5		
		0.6	0.009	0.4-0.65		0.15-0.45		
		0.73	0.013	0.4-0.67		0.12-0.48		
		0.88	0.018	0.4-0.66		0.11-0.49		
		1.12	0.03	0.4-0.71		0.1-0.29		
		1.42	0.048	0.35-0.75		0.11-0.3		
		12	2.11 cloud / unsteady intermittent cavitation	0	0	0.45		0.35
1.51				0.055	0.4-0.5		0.25-0.4	

^a Note that $L_c^{max} = L_c$ for all steady regimes.

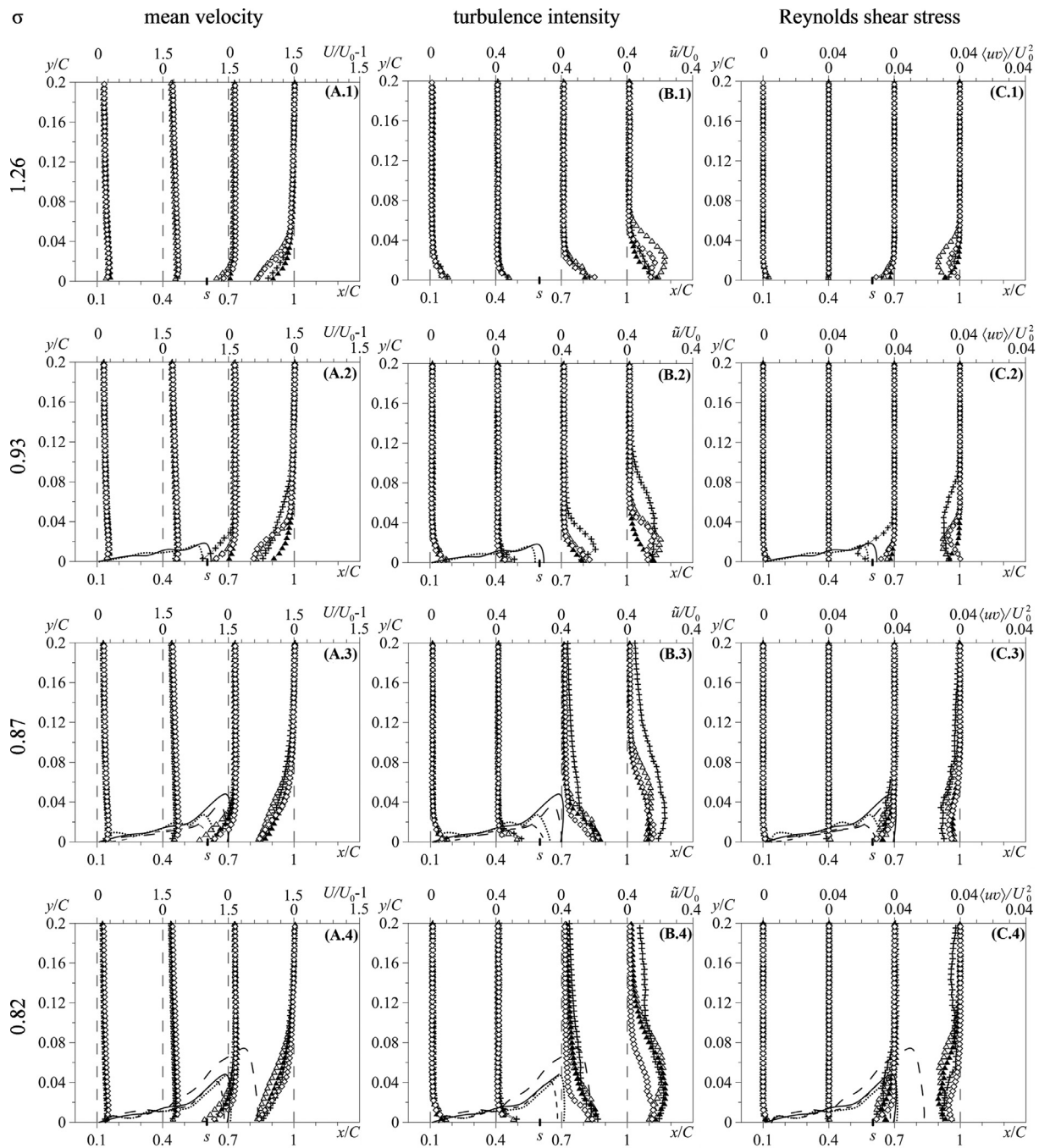


Fig. 3. Downstream evolution of the streamwise components of (A) the mean velocity (in form of the velocity defect) and (B) turbulence intensity (r.m.s.) and (C) the shear component of the Reynolds stress over the suction side of the guide vane model at the attack angle $\alpha = 3^\circ$ for the following flow conditions: (1) $\sigma = 1.26$ when (Δ) $U_{inj}/U_0 = 0.64$ ($C_\mu = 0.01$) and (\blacktriangle) $U_{inj}/U_0 = 1.32$ ($C_\mu = 0.042$) (subcavitating flow), (2) $\sigma = 0.93$ when (Δ) $U_{inj}/U_0 = 0.65$ ($C_\mu = 0.01$) and (\blacktriangle) $U_{inj}/U_0 = 1.26$ ($C_\mu = 0.038$) (transitional regime / travelling bubbles), (3) $\sigma = 0.87$ when (Δ) $U_{inj}/U_0 = 0.73$ ($C_\mu = 0.013$) and (\blacktriangle) $U_{inj}/U_0 = 1.28$ ($C_\mu = 0.039$) (cavitation surge / transitional regime) and (4) $\sigma = 0.82$ when (Δ) $U_{inj}/U_0 = 0.75$ ($C_\mu = 0.013$) and (\blacktriangle) $U_{inj}/U_0 = 1.25$ ($C_\mu = 0.037$) (cavitation surge). Symbols (+) correspond to the regime without injection, (\diamond) show the distributions for the GV without modification. The solid and broken curves represent interfaces of the sheet cavities when they reach their maximum size: dots ($\bullet\bullet\bullet\bullet\bullet$) – $U_{inj}/U_0 = 0$ for all the regimes when the cavity exists, short dashes (– – –) – $U_{inj}/U_0 = 0.73$ and 0.75 ($C_\mu = 0.013$) when $\sigma = 0.87$ and 0.82 , long dashes (— —) – $U_{inj}/U_0 = 1.28$ and 1.25 ($C_\mu = 0.039$ and 0.037) when $\sigma = 0.87$ and 0.82 , solid line (—) is for the unmodified GV. s denotes the position of the slot channel in the foil surface. The flow direction is from the left.

nus $C =$ more than twice those for the injection-free case, so that $\tilde{u}/U_0 = 0.23$ ($x/C = 1$; $y/C = 0.024$) (Fig. 3-B.1), with their amplitude changed much less close to the wall. The behavior of the shear stress with injection is quite similar: at low injection rates, it rises as much as two times in the same point ($x/C = 1$; $y/C = 0.024$) and match almost completely at the wall (e.g., see Fig. 3-C.1). Thus, the low-speed injection leads to forced turbulization of the BL. An in-

crease of the injection rate up to $U_{inj}/U_0 = 1.32$ ($C_\mu = 0.042$) causes changes in distributions of the velocity characteristics so that they become more uniform than the ones in the injection-free case. In the cross-section $x/C = 1$, $|(U - U_0)|/U_0$ decreases from 0.59 to 0.48 near the GV surface (Fig. 3-A.1) and the intensity of turbulent fluctuations and the amplitude of the Reynolds shear stress become two times smaller within the BL (Fig. 3-B.1 and C.1). A decrease of

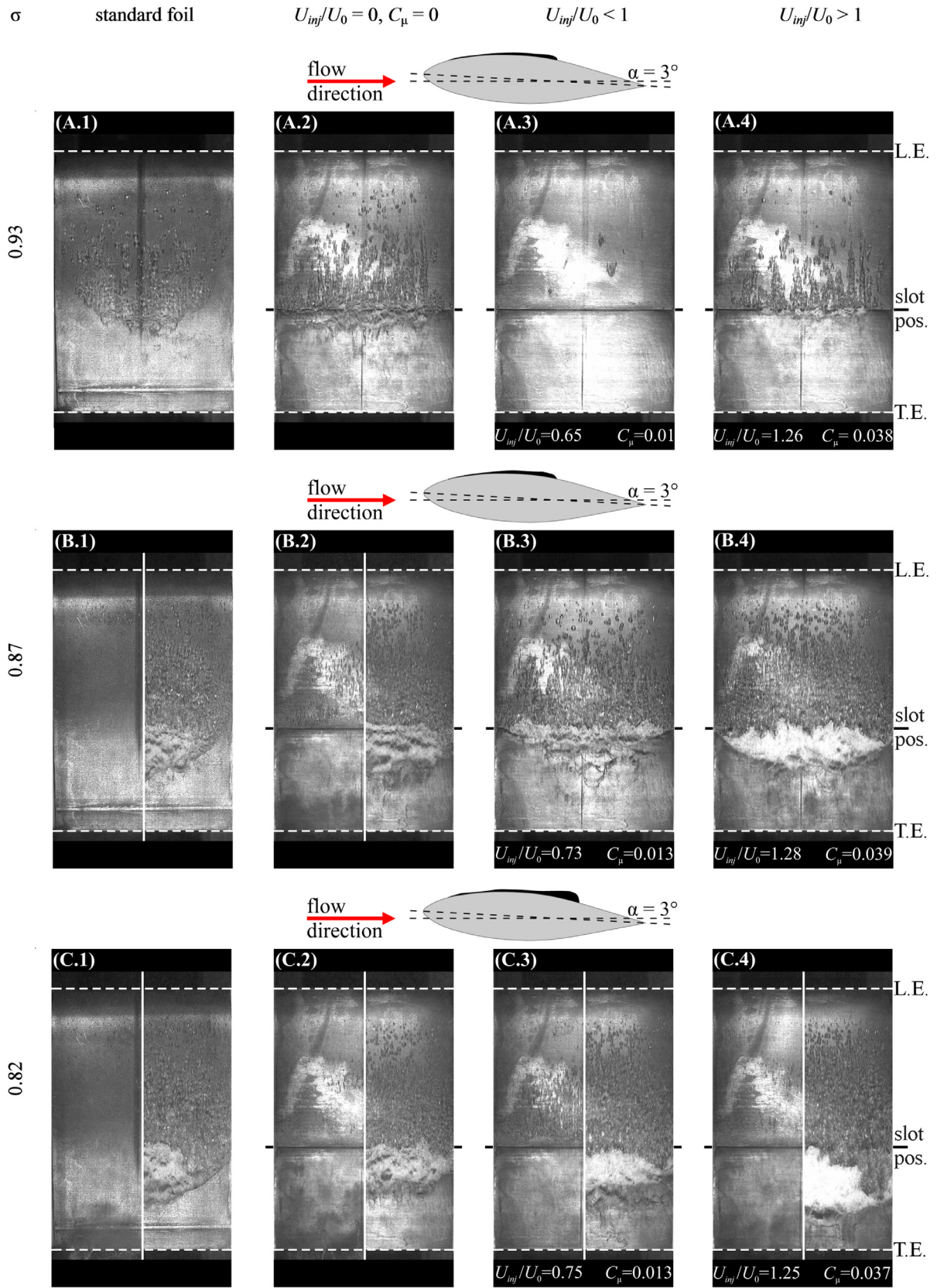


Fig. 4. Instantaneous images of partial cavities (top view) on the suction side of the (1) standard (without the slot) and (2, 3, 4) modified GV model at the attack angle $\alpha = 3^\circ$ for the following conditions: (A) $\sigma = 0.93$ when (2) $U_{inj}/U_0 = 0$ ($C_\mu = 0$), (3) $U_{inj}/U_0 = 0.65$ ($C_\mu = 0.01$) and (4) $U_{inj}/U_0 = 1.26$ ($C_\mu = 0.038$) (transitional regime / travelling bubbles), (B) $\sigma = 0.87$ when (2) $U_{inj}/U_0 = 0$ ($C_\mu = 0$), (3) $U_{inj}/U_0 = 0.73$ ($C_\mu = 0.013$) and (4) $U_{inj}/U_0 = 1.28$ ($C_\mu = 0.039$) (cavitation surge / transitional regime) and (C) $\sigma = 0.82$ when (2) $U_{inj}/U_0 = 0$ ($C_\mu = 0$), (3) $U_{inj}/U_0 = 0.75$ ($C_\mu = 0.013$) and (4) $U_{inj}/U_0 = 1.25$ ($C_\mu = 0.037$) (cavitation surge). For unsteady flow conditions, half images indicating two phases of the attached cavity evolution are shown together in the same picture when (left) it has the shortest (at the moment whereupon the cavity starts to grow) and (right) the longest length (just before the cavity interface breakup). The flow direction is from the top. Above is a side-view flow schematic. For details of the regime time dynamics, see complementary videos available at [doi:10.1016/j.ijmultiphaseflow.2017.11.002](https://doi.org/10.1016/j.ijmultiphaseflow.2017.11.002): movies 1 and 2 correspond to the regimes shown in Fig. 4-A and B, respectively.

both the intensity of velocity fluctuations and the shear stress in absolute magnitude indicates a drag reduction of the hydrofoil.

3.1.2. Transitional cavity / travelling bubbles

When the cavitation number is reduced to $\sigma = 1.04$, cavitation is initiated on the suction side of the modified GV model at the distance of roughly 0.11C from its leading edge in form of separate transient bubbles. For $\sigma = 0.93$, the cavitation area is extended downstream to 0.58C (Fig. 4-A.2). Thus, the streamwise dimension of the cavitating area is $L_C = 0.47C$. In case of the standard GV profile, the cavitation area extension almost coincides with the one on the modified hydrofoil, $L_C = 0.51C$ (cf. Fig. 4-A.1 and A.2). The maximum size of travelling bubbles D_B on the standard GV shape turns out to be larger (2.6 mm) than that on the modified foil (1.9 mm). This difference is probably linked with the fact that the experiments on the two shapes were conducted at periods separated substantially in time, so their surface properties, such as wettability and roughness, could somewhat differ due to corrosion and oxidation. Anyhow, this circumstance does not seem to be critical for the problem under consideration as it influences only the flow regimes at cavitation onset. In the injection-free case, a pressure jump that must exist over the foil surface when crossing the slot can hamper streamwise expansion of the cavitation area and make the bubbles to collapse. Vortices originating and developing in the separated BL behind the nozzle presumably due to disturbances caused by the collapsing bubbles entrap clouds of microbubbles arisen during these collapses and transfer them downstream where they eventually dissipate (Fig. 4-A.2). When a low-speed wall jet is generated, the initially observed transitional regime³ of cavitating flow transforms into the typical transient bubble cavitation. An example of this modification of the flow pattern is presented in Fig. 4-A.3 for the relative jet velocity of $U_{inj}/U_0 = 0.65$ ($C_\mu = 0.01$). As seen, the injection results in an abrupt reduction in the spatial density of travelling bubbles and a growth of their maximum size up to $D_B = 5.4$ mm when $U_{inj}/U_0 = 0.79$ ($C_\mu = 0.015$) (see Table 4). The bubbles become larger since they remain unaffected by others during a longer time interval due to their reduced density. The LIF visualization shows that, in this regime, the wall jet is stable in time (Fig. 5-A.1) and spanwise uniform (Fig. 5-A.2). Consequently, the only reason for the decay of the spatial density of transient bubbles is an increase of the local pressure⁴ over the GV surface because of the injection but not, as one could expect, alternating jumps and drops of the local pressure (Franc and Michel, 1988) that could be, for instance, caused by pulsations of the flow rate of the generated jet. The sensor measured pressure inside the nozzle chamber registered no pressure pulsations for all U_{inj}/U_0 considered, which proves the above statement. A rise in the velocity of the injected liquid up to $U_{inj}/U_0 = 1.26$ ($C_\mu = 0.038$)

³ Recall that this cavitation regime is intermediate between a steady cavity flow and unsteady cavitation conditions. In the latter case, autooscillations of an attached cavity length occur and, in the case of cloud cavitation, large-scale vapor clouds are periodically shed downstream. A transitional cavity is characterized by intermittent shedding of relatively small clouds and larger horseshoe-shaped ones from its closure. In the case when cavitation occurs in form of travelling bubbles, the transitional cavity is comprised of a large number of transient bubbles that grow, interact with each other and merge into larger structures but, once they reach a higher-pressure region, break up into smaller clouds consisting of vapor microbubbles.

⁴ It is clear that the wall jet discharging with a velocity lower than the local flow velocity (low-speed jet) slows the primary flow down nearby the injection point. The flow deceleration leads, in turn, to an increase of the local pressure in some region close to the slot position and, therefore, prompts a pressure growth over the whole GV suction side, which is the reason for the cavity shortening or even its disappearance. In contrast, the high-speed jet accelerates the liquid layers lying upstream of the slot owing to the ejection effect and reduces the pressure rise at the slot. Thus, the high-speed injection causes a decrease of the average pressure level over the hydrofoil and, as a result, makes the cavity to elongate.

leads to an opposite effect: the spatial density of travelling bubbles grows (Fig. 4-A.4) and the maximum bubble diameter predictably decreases ($D_B = 2.9$ mm), with the flow regime unchanged. The amount of the vapor phase, however, appears to be still lower compared to the one for the injection-free conditions (Fig. 4-A.2).

In this regime, distributions of the mean velocity and turbulence characteristics over the standard GV foil differ insignificantly from those for the subcavitating flow. However, for the modified GV profile, considerable changes in the distributions can be observed even in the case without forcing when the cavitation becomes more developed (cf. Fig. 3-A.1, A.2, B.1, B.2, C.1 and C.2). For instance, δ_{BL} increases from 0.03C in the cross-section $x/C = 0.7$ and 0.05C at $x/C = 1$ (subcavitating flow, Fig. 3-A.1) up to 0.04C and 0.08C in the same sections, respectively (Fig. 3-A.2). The mean velocity turns out to be noticeably lower in the near-wall region ($y/C < 0.1$) as compared to the subcavitating regime, so that its minimum reaches $U^{min}/U_0 = 0.43$ at $x/C = 0.7$ and $U^{min}/U_0 = 0.28$ at $x/C = 1$. Meanwhile, turbulent fluctuations within the BL rise up to $\tilde{u}/U_0 = 0.21$ ($x/C = 0.7$) and 0.17 ($x/C = 1$) (Fig. 3-B.2). The Reynolds shear stress expectedly remains negative and diminishes to $\langle uv \rangle / U_0^2 = -0.022$ ($x/C = 0.7$) and -0.01 ($x/C = 1$) (Fig. 3-C.2). This seems to occur because, in the transitional regime (Fig. 4-A.2), the transient bubbles regularly reaching the 'backward-facing step' disturb strongly the BL right before its separation. This disturbed layer reattaches to the wall downstream, causing a further turbulence intensification. When the injection with the low velocity of $U_{inj}/U_0 = 0.65$ ($C_\mu = 0.01$) is started, δ_{BL} is reduced practically two times down to 0.025C ($x/C = 0.7$) and 0.045C ($x/C = 1$) compared to the injection-free case (Fig. 3-A.2). The maximum of the velocity fluctuations and the minimum of the shear stress shift from $y/C = 0.015$ at $x/C = 0.7$ closer to the wall ($y/C = 0$) and their amplitudes decrease significantly, so $\tilde{u}/U_0 = 0.12$ (halved) and $\langle uv \rangle / U_0^2 = -0.005$ (four and a half times smaller) (Fig. 3-B.2 and C.2). As discussed above, in this regime (Fig. 4-A.3) injection with a low velocity causes a transformation of the cavitation type into travelling bubbles that almost do not interact with each other because of their low spatial density and rarely reach the 'backward-facing step' as shown in Fig. 5-A.1. Thus, the BL upstream of the nozzle exit must be only weakly disturbed and, consequently, turbulence within the downstream BL appears to be of a less intensity (Fig. 3-B.2). At $x/C = 1$, the corresponding peak of the turbulence intensity and the valley of the Reynolds shear stress are also shifted to the surface but their values practically coincide with those for the unforced case: $\tilde{u}/U_0 = 0.2$ and $\langle uv \rangle / U_0^2 = -0.01$ (Fig. 3-B.2 and C.2). An increase of the injection rate up to $U_{inj}/U_0 = 1.26$ ($C_\mu = 0.038$) affects the velocity characteristics very little in the cross-section $x/C = 0.7$ as compared to the low-speed injection conditions. However, near the trailing edge, the high-speed injection makes the modulus of the velocity defect to diminish from $|(U - U_0)/U_0| = 0.92$ for the unmodified GV foil to 0.45, and results in a drop of the level of turbulent fluctuations and the shear stress more than two times. Hence, we can infer that the high-speed injection is more preferable from the standpoint of flow hydrodynamics.

3.1.3. Unsteady cavitation / transitional cavity

A further minor decrease of σ to 0.87 results in destabilization of the cavitating flow over both GV profiles when no forcing is applied. An attached cavity begins to oscillate at the reduced frequency $St = fL_C^{max}/U_0 \approx 0.1$, where f is the measured frequency of pressure pulsations and L_C^{max} is the maximum length of cavitation area (attached cavity) (Fig. 4-B.1 and B.2). For the modified hydrofoil, the streamwise dimension of the cavitation area changes from zero when the cavitation vanishes completely to $L_C^{max} = 0.51C$ in its maximum. The travelling bubbles become small ($D_B = 1.6$ mm) (Fig. 4-B.2). For these flow conditions, the low-speed ($U_{inj}/U_0 < 1$)

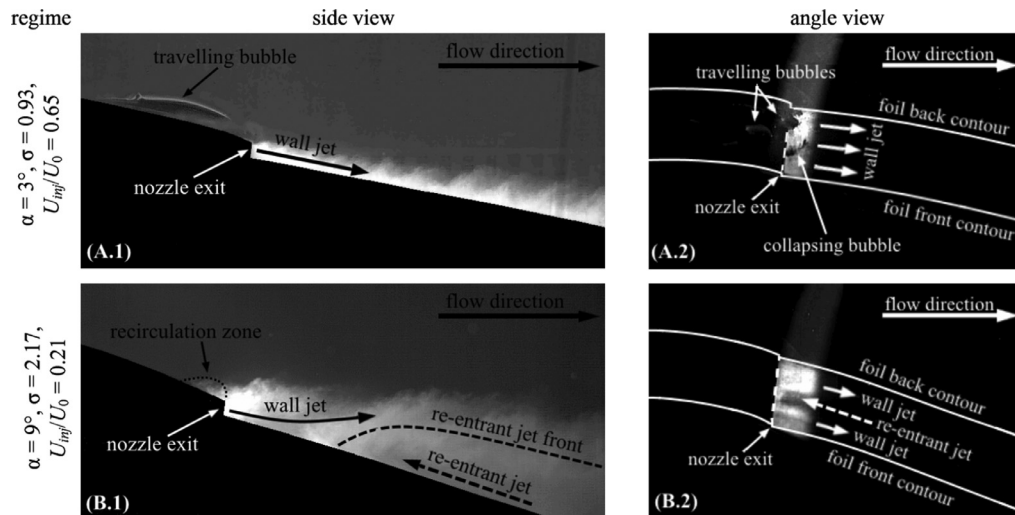


Fig. 5. Instantaneous LIF images of the wall jet discharging from the slot channel (marked as nozzle exit) with indicated flow structure captured (1) from the side and (2) at the angle of 25° in the vertical direction when (A) $\alpha = 3^\circ$, $\sigma = 0.93$, $U_{inj}/U_0 = 0.65$ ($C_\mu = 0.01$) and (B) $\alpha = 9^\circ$, $\sigma = 2.17$, $U_{inj}/U_0 = 0.21$ ($C_\mu = 0.001$). For details of the regime time dynamics, see complementary videos available at [doi:10.1016/j.ijmultiphaseflow.2017.11.002](https://doi.org/10.1016/j.ijmultiphaseflow.2017.11.002): movies 1 and 3 correspond to the regimes shown in Fig. 5-A and B, respectively.

injection of liquid allows the flow stabilization (e.g., see Fig. 4-B.3). The cavitation area length initially diminishes to $L_C = 0.46C$ but then gradually grows to $0.59C$ with the injection rate and the maximum size of transient bubbles increases up to $D_B = 3.6\text{ mm}$ for $U_{inj}/U_0 = 0.85$ ($C_\mu = 0.017$) (see Table 4). Thus, the regime of the cavitating flow over the modified GV section becomes transitional like that presented in Fig. 4-A.2. The hydroacoustic measurements confirm this observation showing that the amplitude of pressure pulsations for the fundamental harmonic A_0 occurring initially at frequency of $f_0 = 20.9\text{ Hz}$ drops dramatically with the injection rate and turns out to be only slightly above the noise level for $U_{inj}/U_0 > 0.4$, with f_0 changed to 18.7 Hz (see Fig. 6-A). It is worth noting that, in the case when $U_{inj}/U_0 = 0.73$ (Fig. 4-B.3), the value of the jet momentum coefficient C_μ is merely 0.013, which indicates the smallness of the energy consumed to suppress the flow unsteadiness in comparison with the energy of the flow itself. A subsequent increase of U_{inj}/U_0 up to 1.28 (Fig. 4-B.4) no longer leads to modification of the regime of cavitating flow – it remains transitional – but slightly augments the spatial density of transient bubbles and elongates the cavitating area, diminishing the transient bubbles in size down to $D_B = 2.6\text{ mm}$. When the cavitation number is decreased again to $\sigma = 0.82$, the forcing does not change the cavitation pattern anymore (see Fig. 4-C.2, C.3 and C.4). The cavitating flow keeps its unsteady behavior and the cavitation sheet continues to oscillate ($St \approx 0.1$), although the streamwise dimension of the cavitation area somewhat decreases from $L_C^{\max} = 0.58C$ for $U_{inj}/U_0 = 0$ to $0.52C$ for $U_{inj}/U_0 = 0.25$ ($C_\mu = 0.002$) and after that progressively increases to $0.7C$ for $U_{inj}/U_0 = 1.25$ ($C_\mu = 0.037$). In this regime, the injection has almost no effect on the size of the transient bubbles ($D_B \approx 2\text{ mm}$, see Table 4). Nevertheless, the hydroacoustic measurements show that the amplitude of pressure pulsations drops as U_{inj}/U_0 is gradually increased and achieves its minimum when U_{inj}/U_0 is about 0.75 ($C_\mu = 0.013$). Afterwards, it grows almost linearly with the injection velocity (Fig. 6-B). The pressure transducer in the nozzle chamber appeared to be also sensitive to these pressure pulsations but did not reveal anything new. Hence, at small attack angles, the low-speed injection is more effective than the high-speed one for cavitation hampering and suppression of instabilities or at least reduction of the amplitude of pressure pulsations associated with the cavitation unsteadiness.

As for the steady flow conditions, in the unsteady regimes the liquid injection shows almost no impact on the profiles of the mean and fluctuating velocities nor the shear stress upstream of the ‘backward-facing step’ (cf. the profiles in the cross-sections $x/C = 0.1$ and 0.4 in Fig. 3). This means that the interaction of an attached cavity with the generated wall jet upstream of the slot position can occur only due to changes in the local pressure distribution along the foil surface and is independent of the turbulent structure, which partly proves the conjecture on the pressure rise over the GV surface due to the low-speed injection drawn above from the visual data (see Section 3.1.2). Under the unsteady flow conditions at $\sigma = 0.87$ and $\sigma = 0.82$, for all the cases presented in Fig. 3-A.3 and A.4, including the injection-free one, δ_{BL} increases up to $0.05C$ at $x/C = 0.7$ and $0.11C$ at $x/C = 1$ with respect to those at $\sigma = 0.93$. As seen, an additional momentum supply does not influence δ_{BL} but makes the mean velocity to decrease to some extent in the near-wall region ($y/C < 0.1$), especially at the low injection rates with $U_{inj}/U_0 = 0.73$ ($C_\mu = 0.013$) at $\sigma = 0.87$ and $U_{inj}/U_0 = 0.75$ ($C_\mu = 0.013$) at $\sigma = 0.82$. For these injection velocities, the mean velocity U becomes lesser by $0.4U_0$ at $x/C = 0.7$ and $0.1U_0$ at $x/C = 1$ for $\sigma = 0.87$ and by $0.21U_0$ and $0.15U_0$ in the same cross-sections for $\sigma = 0.82$ compared to the unforced case (see Fig. 3-A.3 and A.4). It can be noted that, when the transition to unsteady cavitation regimes occurs, the mean velocity distributions appear to be very similar for both modified and standard GV shapes (Fig. 3-A.3 and A.4) but such a statement cannot be made for the turbulent characteristics (see Fig. 3-B.3, B.4, C.3 and C.4). For instance, at $\sigma = 0.87$ the turbulence intensity is higher ($\tilde{u}/U_0 = 0.22$ at $x/C = 1$) for the modified GV foil without injection than the ones for the standard GV profile and the modified GV model with the low- or high-speed injections ($\tilde{u}/U_0 \approx 0.15$) in the same cross-section (Fig. 3-B.3). This is apparently linked with the difference in shapes of the two hydrofoils, especially due to the ‘backward-facing step’ (Fig. 2), and the flow regime transformation to the transitional one when the injection rate is nonzero (Fig. 4-B.3). Thus, we can infer that, under unsteady flow conditions at $\sigma = 0.87$, the injection allows a reduction of the turbulence intensity, at best approaching the level of turbulent fluctuations to that for the standard hydrofoil. At $\sigma = 0.82$, neither the low- nor high-speed injections are able to make the distributions of the turbulent characteristics closer to those for the standard GV model (Fig. 3-B.4 and C.4). So, in the cross-section $x/C = 1$, $\tilde{u}/U_0 = 0.12$ and 0.18 for the stan-

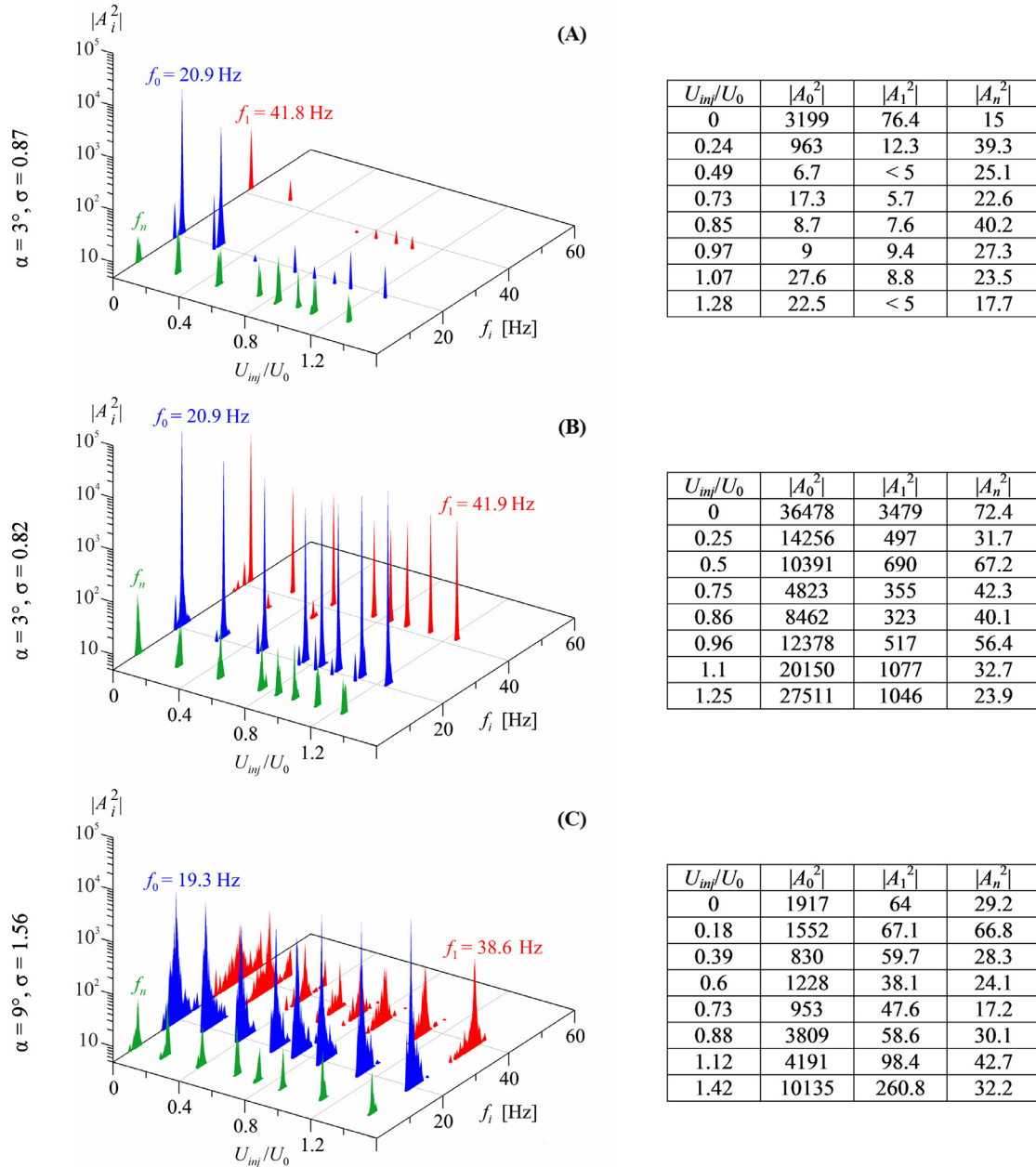


Fig. 6. Power spectra of pressure pulsations (fast Fourier transform) dependence on the injection velocity (left) and tables containing actual values of the pressure pulsation amplitudes at various injection velocities (right) for the modified GV model under unsteady cavitating flow conditions when (A) $\alpha = 3^\circ, \sigma = 0.87$, (B) $\alpha = 3^\circ, \sigma = 0.82$ and (C) $\alpha = 9^\circ, \sigma = 1.56$. Here, f_0, f_1 are frequencies and A_0, A_1 are non-dimensional amplitudes for the fundamental and first higher harmonics, respectively. $f_n \approx 7.7$ Hz is the natural frequency of the cavitation tunnel at all regimes, including non-cavitating, independent of the injection rate and even in the case of free test channel (i.e., without hydrofoil) and A_n is its non-dimensional amplitude that is substantially smaller than A_0 for unsteady flow conditions.

standard and modified vanes, respectively, independently of the injection rate (see Fig. 3-B.4). The distributions of the Reynolds stress in general repeat the behavior of the turbulence intensity except for the sign (Fig. 3-C.4). As seen in the visual data (Fig. 4-C.3 and C.4), at this regime the injection effect on the attached cavity is also weakly pronounced. This is in accordance with the above conclusions concerning the effectiveness of the low- and high-speed injections to hinder the cavitation development and enhance the hydrodynamic characteristics of the GV model at low attack angles.

3.2. Large attack angle ($\alpha = 9^\circ$)

3.2.1. Cavitation sheet / subcavitating flow

At the higher incidence angle, the hydrodynamic structure of the subcavitating flow ($\sigma = 2.82$) around the modified GV model

substantially differs from that at the smaller inclination ($\sigma = 1.26$), similar to the standard foil. The BL turns out to be thicker (cf. Figs. 3-A.1 and 7-A.1) and more turbulent (cf. Figs. 3-B.1 and 7-B.1, 3-C.1 and 7-C.1) with respect to the case of $\alpha = 3^\circ$, though the mean flow velocity U_0 is reduced as the attack angle is increased. At $\alpha = 9^\circ$, δ_{BL} on the modified GV section grows up to 0.04C at $x/C = 0.7$ and 0.1C at $x/C = 1$ (Fig. 7-A.1) as compared to 0.03C and 0.045C for $\alpha = 3^\circ$ at the same cross-sections (Fig. 3-A.1). At the trailing edge ($x/C = 1$), the maximum of turbulent fluctuations ($\tilde{u}/U_0 = 0.19$) and the minimum of the Reynolds shear stress ($\langle uv \rangle / U_0^2 = -0.015$) appear to be higher and lower, respectively, than those for $\alpha = 3^\circ$ ($\tilde{u}/U_0 = 0.16$ and $\langle uv \rangle / U_0^2 = -0.007$), both shifted away from the wall to $y/C = 0.07$ (cf. Figs. 3-B.1 and 7-B.1, 3-C.1 and 7-C.1). As found earlier by Timoshevskiy et al. (2016), at

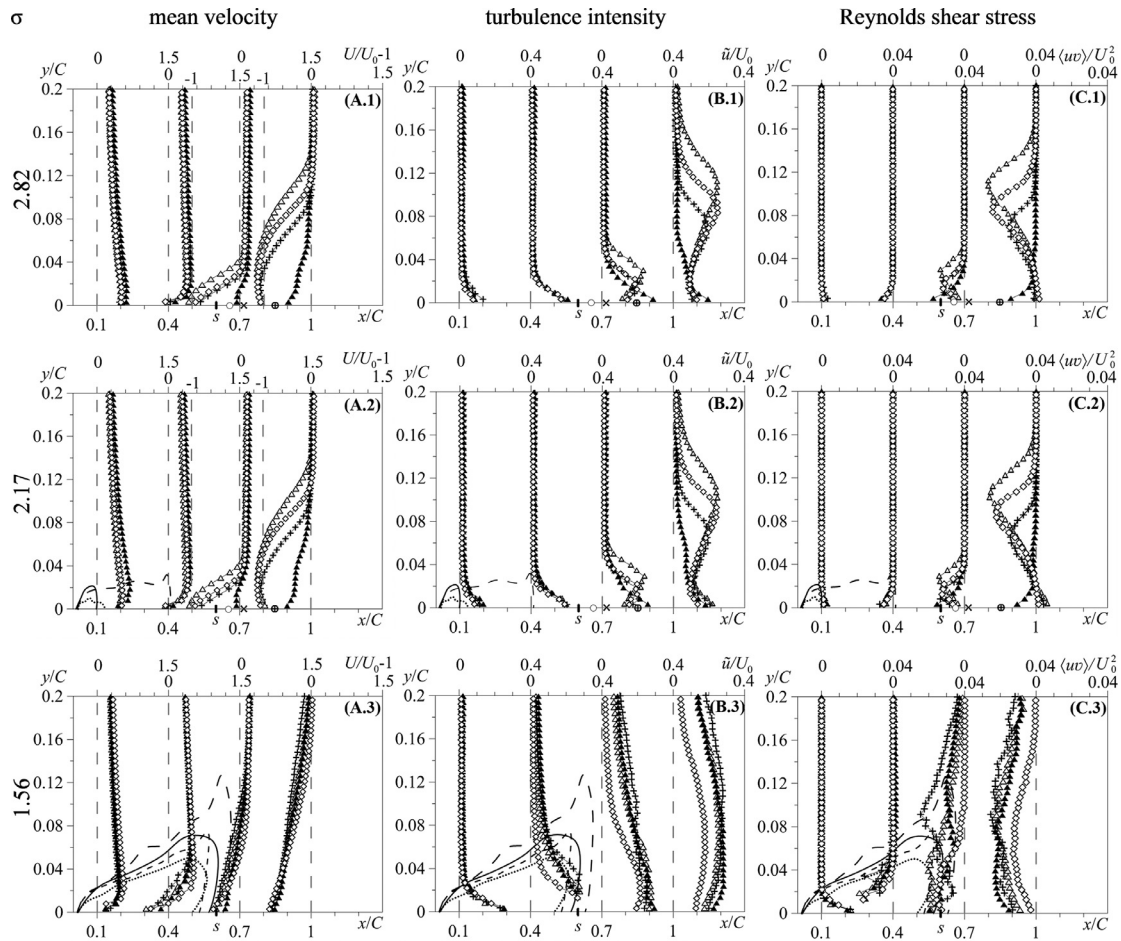


Fig. 7. Downstream evolution of the streamwise components of (A) the mean velocity (in form of the velocity defect) and (B) turbulence intensity (r.m.s.) and (C) the shear component of the Reynolds stress over the suction side of the guide vane model at the attack angle $\alpha = 9^\circ$ for the following conditions: (1) $\sigma = 2.82$ when (Δ) $U_{inj}/U_0 = 0.22$ ($C_\mu = 0.001$) and (\blacktriangle) $U_{inj}/U_0 = 1.66$ ($C_\mu = 0.066$) (subcavitating flow), (2) $\sigma = 2.17$ when (Δ) $U_{inj}/U_0 = 0.21$ ($C_\mu = 0.001$) and (\blacktriangle) $U_{inj}/U_0 = 1.55$ ($C_\mu = 0.058$) (sheet cavity / subcavitating flow) and (3) $\sigma = 1.56$ when (Δ) $U_{inj}/U_0 = 0.88$ ($C_\mu = 0.018$) and (\blacktriangle) $U_{inj}/U_0 = 1.42$ ($C_\mu = 0.048$) (unsteady cavity). Symbols (+) correspond to the regime without injection, (x) show the distributions for the GV without modification. The solid and broken curves represent interfaces of the sheet cavities when they reach their maximum size: dots (.....) - $U_{inj}/U_0 = 0$ for all the regimes when the cavity exists, short dashes (- -) - $U_{inj}/U_0 = 0.88$ ($C_\mu = 0.018$) when $\sigma = 1.56$, long dashes (— —) - $U_{inj}/U_0 = 1.55$ and 1.42 ($C_\mu = 0.058$ and 0.048) for $\sigma = 2.17$ and 1.56 , solid line (——) is for the unmodified GV. The location of flow separation is marked by symbol (\oplus) when $U_{inj}/U_0 = 0$ ($C_\mu = 0$) and (\odot) when $U_{inj}/U_0 = 0.21$ ($C_\mu = 0.001$) for $\sigma = 2.83$ and 2.17 , symbol (x) corresponds to similar regimes for the unmodified GV. s denotes the position of the slot channel in the foil surface. The flow direction is from the left.

$\alpha = 9^\circ$ a subcavitating flow separates from the surface of the standard GV profile approximately at $x/C = 0.72$. When no injection is applied, the BL separation point on the modified GV model is displaced downstream to $x/C = 0.85^5$ (Fig. 7-A.1), due to delayed BL turbulization linked with the difference in the foil shapes (Fig. 2) similar to $\alpha = 3^\circ$ discussed in Section 3.1.1. As a result, the BL on the modified foil occurs to be thinner (Fig. 7-A.1) and less turbulent (Fig. 7-B.1 and C.1) compared to the standard one. The low-speed injection with $U_{inj}/U_0 = 0.22$ ($C_\mu = 0.001$) makes the separation point to move upstream to $x/C = 0.66$, whereas the high-speed one with $U_{inj}/U_0 = 1.66$ ($C_\mu = 0.066$) shifts it downstream to the GV trailing edge ($x/C = 1$). The reason of the separation point translocation is the primary flow deceleration or acceleration by the low/high-speed injection (details are provided in Section 3.1.2). Correspondingly, the BL thickness, turbulence intensity and Reynolds shear stress in absolute value grow or drop with respect to the unforced flow, depending on the injection conditions. So, at the trailing edge δ_{BL} becomes equal to $0.14C$ and $0.055C$, \bar{u} achieves the values of $0.25U_0$ ($y/C = 0.11$) and $0.19U_0$

($y/C = 0.005$) and $\langle uv \rangle$ changes to $-0.027U_0^2$ ($y/C = 0.11$) and $-0.014U_0^2$ ($y/C = 0.005$) for the low- and high-speed injections, respectively. As observable in Fig. 7, the distributions of the mean and turbulent characteristics are very similar for the subcavitating and sheet-cavity flows at the higher incidence angle, so this discussion is also valid for the latter (Fig. 7-A.2, B.2 and C.2). Thus, based on the above findings we deduce again that, for the steady regimes at higher attack angles, the high-speed wall jet is capable to enhance the hydrodynamic quality of the GV model (measured lift and drag coefficients can be found in Kozhukharov et al., 1985), while the injection with a low velocity causes turbulence intensification over the GV surface, thereby impairing its hydrodynamic characteristics.

The high-speed imaging reveals that, at $\alpha = 9^\circ$ and for $\sigma = 2.3$ in the absence of injection ($U_{inj}/U_0 = 0$), cavitation is initiated right behind the leading edge of both hydrofoils (at $x/C = 0.01$) as a vapor sheet. When $\sigma = 2.17$, the attached cavity length is $L_c/C = 0.08$ and 0.13 for the standard and modified hydrofoils, respectively (Fig. 8-A.1 and A.2). This difference in the cavity lengths is most likely related to the uncertainty of the attack angle setting because, at higher incidences, an incipient attached cavity appears to be very susceptible even to small deviations in the foil inclination.

⁵ The backward flow can be recognized in those plots where the velocity defect $(U - U_0)/U_0 < -1$.

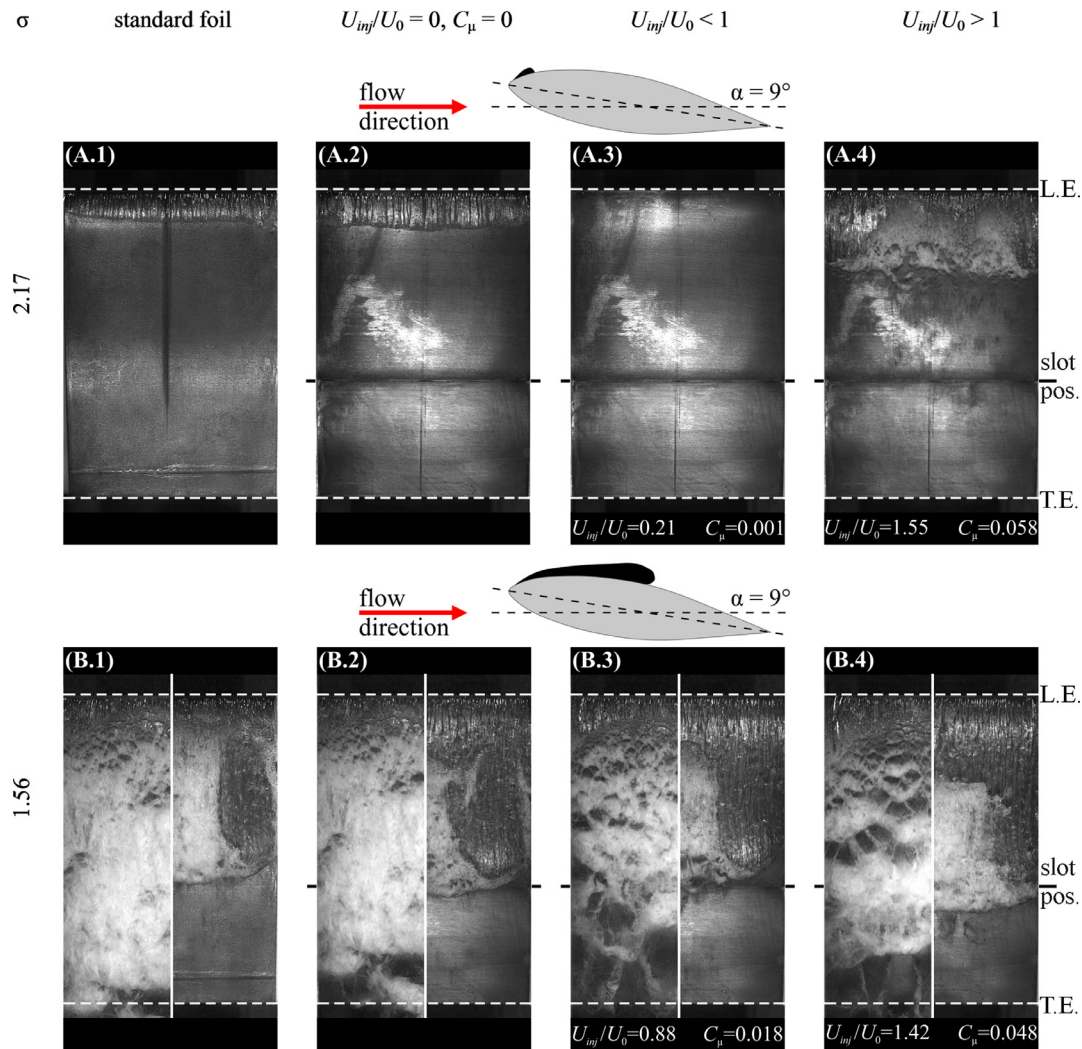


Fig. 8. Instantaneous images of partial cavities (top view) on the suction side of the (1) standard (without the slot) and (2, 3, 4) modified guide vane model at the attack angle $\alpha = 9^\circ$ for the following flow conditions: (A) $\sigma = 2.17$ when (2) $U_{inj}/U_0 = 0$ ($C_\mu = 0$), (3) $U_{inj}/U_0 = 0.21$ ($C_\mu = 0.001$) and (4) $U_{inj}/U_0 = 1.55$ ($C_\mu = 0.058$) (sheet cavity / subcavitating flow) and (B) $\sigma = 1.56$ when (2) $U_{inj}/U_0 = 0$ ($C_\mu = 0$), (3) $U_{inj}/U_0 = 0.88$ ($C_\mu = 0.018$) and (4) $U_{inj}/U_0 = 1.42$ ($C_\mu = 0.048$) (unsteady cavity). For unsteady flow conditions, half images indicating two phases of the attached cavity evolution are shown together in the same picture when (left) it has the shortest (at the moment whereupon the cavity starts to grow) and (right) the longest length (just before the cavity interface breakup). The flow direction is from the top. Above is a side-view flow schematic. For details of the regime time dynamics, see complementary videos available at [doi:10.1016/j.ijmultiphaseflow.2017.11.002](https://doi.org/10.1016/j.ijmultiphaseflow.2017.11.002): movie 3 corresponds to the regime shown in Fig. 8-A.

However, when the cavitation number is decreased and the cavity becomes more developed, its response to these changes becomes less and less pronounced. Once the injection is started, the sheet cavity length diminishes rapidly as the injection rate is increased and vanishes completely at the relative injection velocity slightly above $U_{inj}/U_0 = 0.045$ ($C_\mu = 4 \cdot 10^{-5}$) (see Table 4). Such a high sensitivity of the cavitation sheet to the injection and its anomalous behavior in this regime can be explained as follows. According to LIF visualization (Fig. 5-B.1), the wall jet discharging from the slot nozzle at low flow rates (e.g., see Fig. 8-A.3) exhibits strong disturbances caused by its interplay with a well-developed re-entrant jet moving backward. The re-entrant jet momentum turns out to be occasionally higher than that of the wall jet, forcing the wall jet to deflect from the foil surface, resulting sometimes in its choking inside the nozzle chamber, with a small recirculation zone formed upstream of the slot position (Fig. 5-B.1). However, this is the case only for the central part of the wall jet, whereas no irregularities appear along both sides of the test channel (see Fig. 5-B.2). In addition to the average pressure growth over the GV surface that might be caused by the introduction (constant on average) of the

low-speed wall jet into the primary flow (see Section 3.1.2), it is very likely that there is another reason for the cavitation sheet to disappear. The flow perturbations occurring in the central part of the wall jet might produce disturbances in the local pressure field that propagate upstream and disrupt the steady flow conditions close to the foil leading edge, necessary for the existence of an attached cavity (Franc and Michel, 1988), thereby preventing its formation. This conjecture is indirectly proved by an increase of the amplitude of turbulent fluctuations (Fig. 7-B.2). A subsequent increase of the injection rate does not change the flow pattern until it reaches the threshold of approximately $U_{inj}/U_0 = 0.7$ ($C_\mu = 0.011$). When this critical value is attained, the sheet cavity revives and its length increases with the growth of the wall jet momentum so that, at $U_{inj}/U_0 = 1.07$ ($C_\mu = 0.028$) (not shown) and $U_{inj}/U_0 = 1.55$ ($C_\mu = 0.058$) (Fig. 8-A.4), $L_c/C = 0.17$ and 0.27 , respectively. It seems that, when $U_{inj}/U_0 > 0.7$, the wall jet momentum is sufficient to overcome the re-entrant jet, unchoke the flow from the slot across the whole GV span and, as a result, make the flow conditions upstream of the nozzle invariable. Thus, at higher foil inclinations, the low-speed wall jet appears to be effective again for cavitation

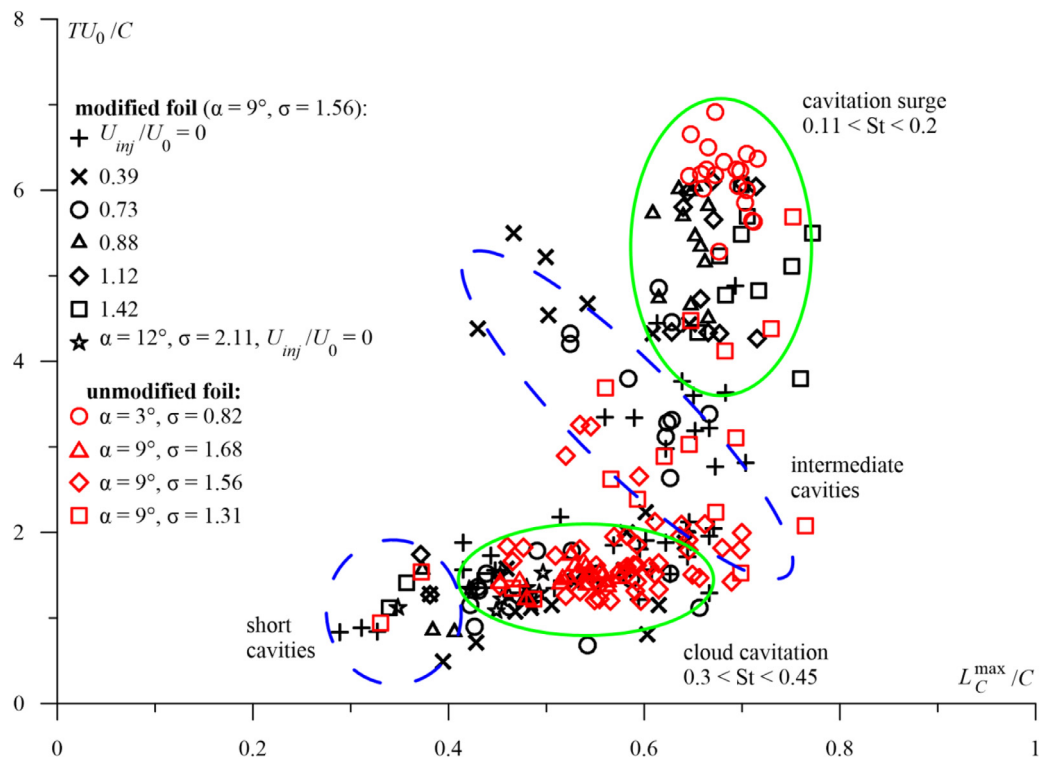


Fig. 9. Periods of the attached cavity pulsations T normalized to the characteristic flow-through time of the GV model C/U_0 against the maximum cavity length for both modified and unmodified hydrofoils. The symbol size was chosen to represent the measurement uncertainty of the quantities for both coordinate axes.

hampering or even its total suppression whereas the high-speed injection provokes a sheet cavity growth and, consequently, leads to a faster transition to unsteady regimes.

3.2.2. Unsteady cavitation

Under unsteady flow conditions (e.g., see Fig. 8-B.2), typical cloud cavitation with $0.3 < St < 0.45$ was never registered on the modified GV model, unlike the standard hydrofoil (Fig. 8-B.1) for which the cloud cavitation occurred in a narrow range on the cavitation number between 1.68 and 1.56 (see Fig. 9). Instead, unsteady intermittent regimes without a pronounced periodicity of the cavity length oscillations and cloud shedding were observed. Such a cavity dynamics is likely to be conditioned by the following. First, since the maximum GV thickness H^{\max} is at $x^{\max} \approx 0.44C$ that is rather remote from the leading edge, the primary flow is contracted at a relatively far distance from the foil leading edge, which, in turn, obstructs a regular development of the re-entrant jet – the main mechanism of the cloud cavitation instability in the present research.⁶ Consequently, the attached cavity becomes longer than it is needed for the conventional cloud cavitation to occur and, thereby, sensitive to pressure variations in the test section (Callenaere et al., 2001). Secondly, the ‘backward-facing step’ on the GV surface represents a barrier for the re-entrant jet and, thus, impedes its development (Kawanami et al., 1997), which requires an additional momentum for the reverse flow to pass it through. All these lead to the conclusion that a cavitation sheet

on the modified GV profile at higher attack angles is susceptible to both types of instabilities – re-entrant jet and cavitation surge (Fig. 9). That is why, at $\sigma = 1.56$ (Fig. 8-B.2), its maximum length changes in the range between $L_C^{\max} = 0.3C$ and $0.7C$ (see Table 4) rather than from $0.4C$ to $0.6C$ as it would be in the case of typical cloud cavitation. Hence, the cavitation behavior in unsteady regimes at higher angles of attack is conditioned by superposition of the two instabilities.⁷ Therefore, frequencies at which these pulsations of the cavity length occur do not fully correspond to the diapason of self-resonant frequencies of any unsteadiness but are dispersed in a wider range. The measured periods of the cavity oscillations shown in Fig. 9 and compared with those for the standard foil confirm this inference. Because of simultaneous receptivity of the cavitation sheet to both instabilities, periods of the cavity length oscillations additionally include cycles with intermediate and shorter cavity lengths compared to the cloud cavitation conditions (Fig. 9). As a result, at high attack angles the generated wall jet appears to be incapable of influencing unsteady cavitation to the extent needed to delay the development of flow instabilities. The low-speed injection brought about only a minor shortening of the cavity length (Fig. 8-B.3 and Table 4) but a twofold reduction of the amplitude of pressure pulsations (Fig. 6-C). Conversely, the high-speed jet leads to a slight extension of the attached cavity (Fig. 8-B.4 and Table 4) and a fivefold growth of the amplitude of pressure pulsations (Fig. 6-C) similar to the case for the small incidence angle (Fig. 6-B). In general, an increase of the attack angle leads to a thickening of the attached cavity, so that, when the cavity vertical dimension becomes larger than the ‘backward-facing step’ height, the step weakly affects the flow evolution facilitating the development of re-entrant jet. Thus, the higher the attack angle is, the less effective the injection will be.

⁶ We presume it is the mechanism associated with development of a re-entrant jet which is responsible for the transition to periodic large-scale cloud cavitation but not the one related to propagation of a bubbly shock. This is because the sheet cavities are comprised of pure vapor phase without gas inclusions and liquid bridges (which is proved by their glossy interface in the visual data). Thus, a high-void-fraction bubbly mixture (that would result in a frothy cavity interface) required for the formation of condensation shocks due to reduced sound speed (Reisman et al., 1998; Ganesh et al., 2016) is practically absent in the cavity separation region.

⁷ It is known (Callenaere et al., 2001) that the instabilities do not interfere.

The mean velocity profiles for the unsteady regime at $\sigma = 1.56$ look quite similar for both foil shapes and are independent of the injection rate (Fig. 7-A.3) but differ remarkably from those for the steady flow conditions at $\sigma = 2.17$ (Fig. 7-A.2). First, in case of the unsteady cavity flow, the mean velocity profiles are smoother because they are averaged over a collection of instants that are dispersed over various stages of the cavity oscillation cycles. Second, no reverse flow downstream of the cavity and, consequently, no stationary BL separation from the surface of both hydrofoils are visible in the graphs (Fig. 7-A.3). For this, there exist two reasons. The first one is that, at this unsteady regime, the flow conditions presumably change too fast to form a separation region for which a longer period of stable evolution seems to be required. The other cause is linked with increased turbulence level within the BL due to additional disturbances produced in the cavity closure, which might delay the flow separation. It is worth noting that in all unsteady regimes considered, the instantaneous velocity distributions within the flow region where a sheet cavity exists (cavity region) were essentially measured at the moments in which local spatial density of the seeding particles used for PIV was sufficient (Kravtsova et al., 2014). This is the case when such a region is almost free of cavitation, i.e. either the cavity size is substantially diminished or the vapor phase is significantly dissipated, so that its local concentration is very low. Thus, the mean velocity and turbulent characteristics within the cavity region turn out to be dependent upon the phase of the cavity growth-reduction cycle. Besides, the sampling range of the instantaneous velocity vectors within the cavity region is significantly decreased with respect to the rest of the flow where cavitation never occurs, which results in an increased measurement error of the statistical quantities (Kravtsova et al., 2014). Unlike the mean velocity, distributions of the turbulent characteristics for the modified and standard GV models differ, irrespective of the injection conditions (Fig. 7-B.3 and C.3). The amplitudes of turbulent fluctuations and the Reynolds shear stress in absolute values appear to be generally one and a half or two times higher for the modified GV profile. So, at $x/C = 1$ $\bar{u}^{\max}/U_0 = 0.27$ and $\langle uv \rangle^{\max}/U_0^2 = -0.025$ compared with $\bar{u}^{\max}/U_0 = 0.17$ and $\langle uv \rangle^{\max}/U_0^2 = -0.012$ for the standard foil. As already discussed, this is directly connected with the difference in geometries of the two vanes (Fig. 2). In general, it can be inferred that the PIV measurements fully confirm the conclusion drawn from the visual observations that the wall jet is practically ineffective for manipulation of unsteady cavitating flow at relatively high angles of attack.

3.3. Summary

Figs. 10 and 11 sum up the observed effects on the cavitating flow management by a wall jet. As seen, the streamwise dimension of the cavitation area in the case of transient bubbles or attached cavity length for cavitation sheet can be successfully reduced at most by 0.25C using the low-speed injection ($U_{inj}/U_0 < 1$) (dark grey region in Fig. 10). The injection appears to be entirely effective for $U_{inj} < U_{inj}^{cr1} = 0.9U_0$, partially effective when $U_{inj}^{cr1} < U_{inj} < U_{inj}^{cr2}$ and ineffective or even harmful for $U_{inj} > U_{inj}^{cr2} = 1.43U_0$ from the standpoint of cavitation hampering, independent of the cavitation parameter and the incidence angle. However, as mentioned above, the high-speed injection allows improvement of the hydrodynamic quality of the hydrofoil by decreasing its drag coefficient and increasing its lift (Kozhukharov et al., 1985). Fig. 10 shows that the most impact of the injection (i.e., the highest diminishing of the cavitation streamwise extent) is achieved for small angles of attack and low injection rates. For higher incidence angles, the present control method becomes less effective but it still allows a reduction of the cavity length by 0.11C at $U_{inj}/U_0 = 0.66$. Likewise, un-

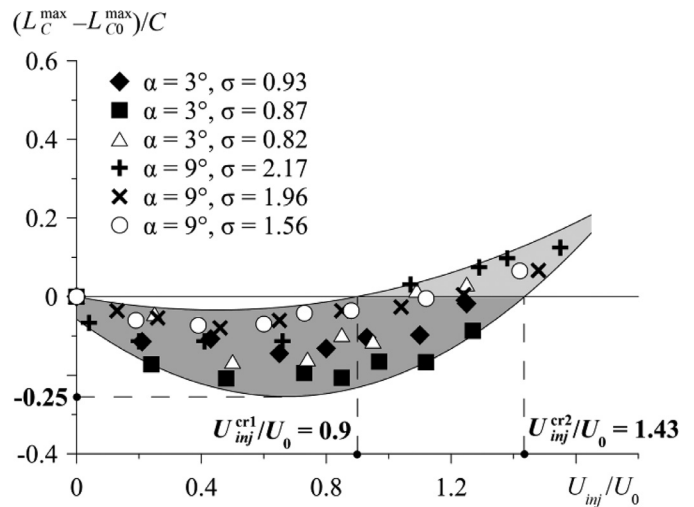


Fig. 10. Dependence of the maximum streamwise dimension of cavitation area (attached cavity length) L_c^{\max} on the modified GV section in comparison with the one on the standard hydrofoil L_{c0}^{\max} upon the injection velocity. Here, U_{inj}^{cr1} and U_{inj}^{cr2} are the first and second critical values of the injection velocity. The symbol size was chosen to represent the measurement uncertainty of the quantities for both coordinate axes.

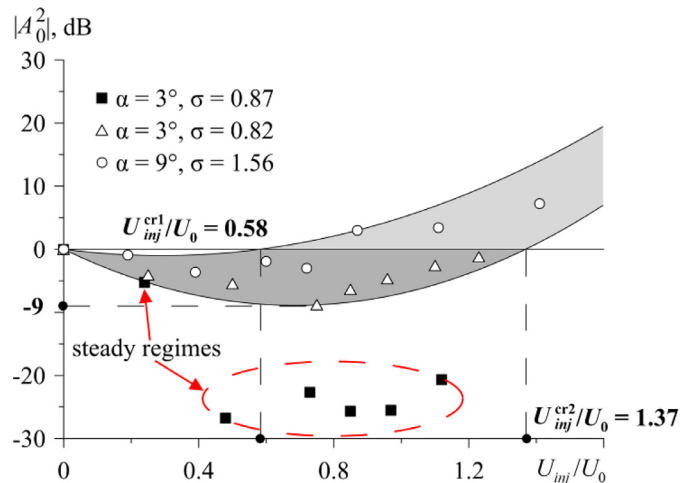


Fig. 11. Dependence of the amplitude of pressure pulsations for the fundamental harmonic with regard to the one for the unforced flow conditions upon the injection velocity. Here, U_{inj}^{cr1} and U_{inj}^{cr2} are the first and second critical values of the injection velocity. The symbol size was chosen to represent the measurement uncertainty of the quantities for both coordinate axes.

der unsteady flow conditions, the amplitudes of pressure pulsations for the fundamental harmonic A_0 (expressed in decibels with respect to the injection-free case) depend upon the wall jet velocity (Fig. 11). In unsteady regimes, the best efficiency of this control technique is reached at small incidences and low injection velocities $0 < U_{inj} < U_{inj}^{cr1} = 0.58U_0$. In particular, when $\alpha = 3^\circ$ and $\sigma = 0.87$, the unsteadiness is shown (Figs. 4-B.3 and 6-A) to be completely suppressed and the amplitude of pressure pulsations falls by 25 dB (Fig. 11). For lower cavitation numbers, A_0 can be decreased only by 9 dB at most. For the higher foil inclination, the amplitude drop appears to be even smaller and does not exceed 5 dB (Fig. 11). It is also worth noting that the peak heights and shapes in the pressure pulsation power spectra differ noticeably for $\alpha = 3^\circ$ and 9° (Fig. 6-B and C). For example, in the injection-free case, the maximum for $\alpha = 3^\circ$ turns out to be 15 times higher and considerably narrower than the one at $\alpha = 9^\circ$. This is because, at the small attack angle, the cavity flow unsteadiness is conditioned

only by the development of cavitation surge instability, whereas at the larger incidence superposition of the cavitation surge and re-entrant jet instabilities occurs (see Section 3.2.2), leading to a dispersion of cavity lengths and periods of its oscillations over a wider range (Fig. 9). Consequently, at higher foil inclinations, the perturbations of local pressure induced by the cavity pulsations turn out to be distributed in a broader frequency range and their amplitudes are depressed. Thus, in practice under similar cavitating conditions, the risk of occurrence of resonance phenomena seems to be considerably lower for the modified GV model.

4. Conclusions

Applying a high-speed imaging, time-resolved LIF visualization, 2D PIV technique and hydroacoustic pressure measurements, a novel method of active control of cavitation has been investigated using a wall jet generated by continuous tangential liquid injection through a spanwise slot in the surface of a two-dimensional hydrofoil and its effectiveness has been assessed. The experiments were carried out on a scaled-down model of guide vanes (GV) of a Francis turbine at the attack angle $\alpha = 3$ and 9° for different regimes, starting from a subcavitating flow and finishing by unsteady regimes with developed attached cavities. The momentum coefficient of the wall jet C_{μ} did not exceed 0.066, which implies that the amount of energy consumed for manipulation is small compared to that of the primary flow. The effects of liquid injection on the cavitation inception and development as well as modification of the attached cavity pattern and cavitating flow regime are considered for different relative strengths of the wall jet defined by the velocity ratio U_{inj}/U_0 . Comparison of the measured distributions of mean velocity and turbulent characteristics around the GV model with slot and the unmodified profile revealed a series of distinctive flow features dictated by the difference in shapes of the two hydrofoils and the liquid injection rates.

At small incidence angles, the low-speed ($U_{inj}/U_0 < 1$) injection was found to mitigate cavitation under steady flow conditions, shortening the streamwise dimension of cavitation area, reducing the spatial density of transient bubbles (simultaneously increasing their size), and, under certain conditions, delaying the evolution of cavitating flow regime and suppressing the development of flow instabilities. This occurs because of a rise of local pressure over the GV surface caused by a slowdown of the primary flow due to the low-speed wall jet nearby the slot position. Besides, the low-speed injection also leads to a growth of turbulence intensity over the GV section and in its wake, which, in turn, increases the foil drag and, thus, impairs its hydrodynamic quality. The high-speed ($U_{inj}/U_0 > 1$) injection is on the contrary more preferable from the standpoint of flow hydrodynamics. However, it causes the cavitation to initiate at higher cavitation numbers as compared to the unforced (without injection) case or, in other words, the flow becomes more cavitation-prone. The reason for this is an acceleration of the liquid layers upstream of the slot owing to the ejection effect and, consequently, a decrease of the average pressure level over the hydrofoil, which makes the cavity to elongate. In most unsteady regimes, this control method turns out to be, however, unable to suppress the flow unsteadiness but allows a substantial drop of the amplitude of pressure pulsations associated with oscillations of the streamwise dimension of an attached cavity. The above findings are in general also valid for larger angles of attack but the higher the incidence angle is, the less effective the implemented control method becomes.

At higher foil inclinations, a stable cavitation sheet can be completely removed from the GV surface by the low-speed injection, namely for 0.045 $\langle U_{inj}/U_0 < 0.7$, when the wall jet and a re-entrant jet counteract continuously. This results in strong disturbances that presumably propagate upstream and destabilize the flow close to

the foil leading edge, which is unfavorable for a sheet cavity to form. When $U_{inj}/U_0 > 1$, in addition to the average pressure drop over the GV section, the wall jet momentum is likely to be sufficient to overcome the re-entrant jet and turn it away from the slot channel, leading to the establishment of steady flow conditions and reappearance of the cavitation sheet. Under unsteady flow conditions, typical cloud cavitation was never registered on the modified GV model. Instead, unsteady intermittent regimes without a pronounced periodicity of the cavity length oscillations and cloud shedding process were observed. Such cavity dynamics is first conditioned by the maximum GV thickness being remote from the leading edge. Thus, the primary flow is contracted over a relatively far distance from the foil leading edge, which, in turn, obstructs a regular development of the re-entrant jet regarded as the main mechanism of the cloud cavitation instability in this study. Consequently, the attached cavity becomes longer than it is needed for the conventional cloud cavitation to occur and, thereby, sensitive to pressure variations in the test section. Secondly, the 'backward-facing step' on the GV surface formed by the slot channel and its lip represents a barrier for the re-entrant jet, which requires an additional momentum for the reverse flow to pass it through. All these lead to the conclusion that a cavitation sheet on the modified GV profile at higher attack angles is susceptible to both types of instabilities – re-entrant jet and cavitation surge – and its behavior is conditioned by their superposition.

In general, the obtained results clearly demonstrate the capability of the implemented method of flow control to manipulate cavitation under certain conditions. The streamwise dimension of the cavitation area in the case of transient bubbles or attached cavity length for cavitation sheet can be successfully reduced at most by 0.25C using the low-speed injection ($U_{inj}/U_0 < 1$). The injection appears to be entirely effective for $U_{inj} < 0.9U_0$, partially effective when $0.9U_0 < U_{inj} < 1.43U_0$ and ineffective or even harmful for $U_{inj} > 1.43U_0$ from the standpoint of cavitation hampering, independent of the cavitation parameter and the incidence angle. In unsteady regimes, the best efficiency of this control technique is reached at small incidences and low injection velocities $0 < U_{inj} < 0.58U_0$. Under such conditions, the unsteadiness can be completely suppressed in some cases, with the amplitude of pressure pulsations falling by 25 dB. However, for lower cavitation numbers and higher attack angles, the pressure pulsations amplitude can be decreased only by 5–9 dB at most. Application of this method in real full-scale industrial facilities can potentially broaden the range of operation conditions of hydraulic equipment and avoid some undesirable unsteady regimes. Moreover, in unsteady regimes at higher angles of attack, dominant frequencies of pressure pulsations associated with oscillations of an attached cavity length and cloud shedding process turn out to be dispersed over a broader range, with their amplitudes substantially decreased (by an order of magnitude or even more), because of simultaneous development of the two cavitation instabilities – cavitation surge and re-entrant jet. Thus, in practice under similar cavitating conditions, the risk of resonance can be considerably reduced in the case of modified GV model. Despite the thorough study performed, further systematic investigations are evidently required for a deeper understanding of the physics of the registered phenomena and optimization of the operating parameters of the control method.

Funding

The research was funded by a grant from the [Russian Science Foundation](#) (Project No. 16-19-00138 supervised by Dr. P.A. Kuibin in IT SB RAS).

Supplementary materials

Supplementary material associated with this article can be found, in the online version, at doi:10.1016/j.ijmultiphaseflow.2017.11.002.

References

- Akcabay, D.T., Chae, E.J., Young, Y.L., Ducoin, A., Astolfi, J.A., 2014. Cavity induced vibration of flexible hydrofoils. *J. Fluids Struct.* 49, 463–484. doi:10.1016/j.jfluidstructs.2014.05.007.
- Ausoni, Ph., Zobeiri, A., Avellan, F., Farhat, M., 2012. The effects of a tripped turbulent boundary layer on vortex shedding from a blunt trailing edge hydrofoil. *ASME J. Fluids Eng.* 134 (5). doi:10.1115/1.4006700, (051207)–11.
- Brandner, P.A., Walker, G.J., Niekamp, P.N., Anderson, B., 2010. An experimental investigation of cloud cavitation about a sphere. *J. Fluid Mech.* 656, 147–176. doi:10.1017/S0022112010001072.
- Callenaere, M., Franc, J.-P., Michel, J.-M., Riondet, M., 2001. The cavitation instability induced by the development of a re-entrant jet. *J. Fluid Mech.* 444, 223–256. doi:10.1017/s0022112001005420.
- Chahine, G.L., Frederick, G.F., Bateman, R.D., 1993. Propeller tip vortex cavitation suppression using selective polymer injection. *ASME J. Fluids Eng.* 115 (3), 497–503. doi:10.1115/1.2910166.
- Chang, N., Ganesh, H., Yakushiji, R., Ceccio, S.L., 2011. Tip vortex cavitation suppression by active mass injection. *ASME J. Fluids Eng.* 133 (11). doi:10.1115/1.4005138, (111301)–11.
- Chatterjee, D., Arakeri, V.H., 1997. Towards the concept of hydrodynamic cavitation control. *J. Fluid Mech.* 332, 377–394. doi:10.1017/s0022112096004223.
- Chatterjee, D., Arakeri, V.H., 2004. Some investigations on the use of ultrasonics in travelling bubble cavitation control. *J. Fluid Mech.* 504, 365–389. doi:10.1017/s0022112004008262.
- Churkin, S.A., Pervunin, K.S., Kravtsova, A.Yu., Markovich, D.M., Hanjalić, K., 2016. Cavitation on NACA0015 hydrofoils with different wall roughness: high-speed visualization of the surface texture effects. *J. Vis.* 19 (4), 587–590. doi:10.1007/s12650-016-0355-9.
- Coutier-Delgosha, O., Devillers, J.-F., Leriche, M., Pichon, T., 2005. Effect of wall roughness on the dynamics of unsteady cavitation. *ASME J. Fluids Eng.* 127 (4), 726–733. doi:10.1115/1.1949637.
- Danlos, A., Ravelet, F., Coutier-Delgosha, O., Bakir, F., 2014. Cavitation regime detection through proper orthogonal decomposition: dynamics analysis of the sheet cavity on a grooved convergent-divergent nozzle. *Int. J. Heat Fluid Flow* 47, 9–20. doi:10.1016/j.ijheatfluidflow.2014.02.001.
- Dean, J.A., 1999. *Lange's Handbook of Chemistry*, 15th ed. McGraw-Hill Inc, New York, p. 1424 ISBN 0-07-016384-7.
- Duttweiler, M.E., Brennen, C.E., 2002. Surge instability on a cavitating propeller. *J. Fluid Mech.* 458, 133–152. doi:10.1017/s0022112002007784.
- Franc, J.P., Michel, J.M., 1988. Unsteady attached cavitation on an oscillating hydrofoil. *J. Fluid Mech.* 193, 171–189. doi:10.1017/s0022112088002101.
- Ganesh, H., Mäkiharju, S.A., Ceccio, S.L., 2016. Bubbly shock propagation as a mechanism for sheet-to-cloud transition of partial cavities. *J. Fluid Mech.* 802, 37–78. doi:10.1017/jfm.2016.425.
- Iga, Y., Hashizume, K., Yoshida, Y., 2011. Numerical analysis of three types of cavitation surge in cascade. *ASME J. Fluids Eng.* 133 (7). doi:10.1115/1.4003663, (071102)–13.
- Peng, X.X., Ji, B., Cao, Y., Xu, L., Zhang, G., Luo, X., Long, X., 2016. Combined experimental observation and numerical simulation of the cloud cavitation with U-type flow structures on hydrofoils. *Int. J. Multiphase Flow* 79, 10–22. doi:10.1016/j.ijmultiphaseflow.2015.10.006.
- Kawakami, D.T., Fuji, A., Tsujimoto, Y., Arndt, R.E.A., 2008. An assessment of the influence of environmental factors on cavitation instabilities. *ASME J. Fluids Eng.* 130 (3). doi:10.1115/1.2842146, (031303)–8.
- Kawanami, Y., Kato, H., Yamaguchi, H., Tanimura, M., Tagaya, Y., 1997. Mechanism and control of cloud cavitation. *ASME J. Fluids Eng.* 119 (4), 788–794. doi:10.1115/1.2819499.
- Kjeldsen, M., Arndt, R.E.A., Effertz, M., 2000. Spectral characteristics of sheet/cloud cavitation. *ASME J. Fluids Eng.* 122 (3), 481–487. doi:10.1115/1.1287854.
- Kozhukharov, P.G., Hadjimikhalev, V.H., Mikuta, V.I., Maltzev, L.I., 1985. Hydrofoil performance control introducing tangential liquid jet. *ASME Fluids Eng. Div.* 31, 67–74.
- Kravtsova, A.Yu., Markovich, D.M., Pervunin, K.S., Timoshevskiy, M.V., Hanjalić, K., 2014. High-speed visualization and PIV measurements of cavitating flows around a semi-circular leading-edge flat plate and NACA0015 hydrofoil. *Int. J. Multiphase Flow* 60, 119–134. doi:10.1016/j.ijmultiphaseflow.2013.12.004.
- Kubota, A., Kato, H., Yamaguchi, H., Maeda, M., 1989. Unsteady structure measurement of cloud cavitation on a foil section using conditional sampling technique. *ASME J. Fluids Eng.* 111 (2), 204–210. doi:10.1115/1.3243624.
- Mäkiharju, S.A., Ganesh, H., Ceccio, S.L., 2015. Effect of non-condensable gas injection on cavitation dynamics of partial cavities. *J. Phys. Conf. Ser.* 656. doi:10.1088/1742-6596/656/1/012161, (012161)–4.
- Reisman, G.E., Wang, Y.-C., Brennen, C.E., 1998. Observations of shock waves in cloud cavitation. *J. Fluid Mech.* 355, 255–283. doi:10.1017/s0022112097007830.
- Tassin Leger, A., Ceccio, S.L., 1998. Examination of the flow near the leading edge of attached cavitation. Part 1. Detachment of two-dimensional and axisymmetric cavities. *J. Fluid Mech.* 376, 61–90. doi:10.1017/s0022112098002766.
- Timoshevskiy, M.V., Churkin, S.A., Kravtsova, A.Yu., Pervunin, K.S., Markovich, D.M., Hanjalić, K., 2016. Cavitating flow around a scaled-down model of guide vanes of a high-pressure turbine. *Int. J. Multiphase Flow* 78, 75–87. doi:10.1016/j.ijmultiphaseflow.2015.09.014.
- Watanabe, S., Tsujimoto, Y., Furukawa, A., 2001. Theoretical analysis of transitional and partial cavity instabilities. *ASME J. Fluids Eng.* 123 (3), 692–697. doi:10.1115/1.1378295.
- Wu, Q., Huang, B., Wang, G., Gao, Y., 2015. Experimental and numerical investigation of hydroelastic response of a flexible hydrofoil in cavitating flow. *Int. J. Multiphase Flow* 74, 19–33. doi:10.1016/j.ijmultiphaseflow.2015.03.023.
- Zarruk, G.A., Brandner, P.A., Pearce, B.W., Phillips, A.W., 2014. Experimental study of the steady fluid-structure interaction of flexible hydrofoils. *J. Fluids Struct.* 51, 326–343. doi:10.1016/j.jfluidstructs.2014.09.009.